arXiv:cond-mat/9706095v1 [cond-mat.supr-con] 10 Jun 1997

Superconducting gap node spectroscopy using nonlinear electrodynamics

Igor Žutić* and Oriol T. Valls
School of Physics and Astronomy and Minnesota Supercomputer Institute
University of Minnesota
Minneapolis, Minnesota 55455-0149

We present a method to determine the nodal structure of the energy gap of unconventional superconductors such as high T_c materials. We show how nonlinear electrodynamics phenomena in the Meissner regime, arising from the presence of lines on the Fermi surface where the superconducting energy gap is very small or zero, can be used to perform "node spectroscopy", that is, as a sensitive bulk probe to locate the angular position of those lines. In calculating the nonlinear supercurrent response, we include the effects of orthorhombic distortion and $a-b$ plane anisotropy. Analytic results presented demonstrate a systematic way to experimentally distinguish order parameters of different symmetries, including cases with mixed symmetry (for example, $d+s$ and $s+id$). We consider, as suggested by various experiments, order parameters with predominantly d-wave character, and describe how to determine the possible presence of other symmetries. The nonlinear magnetic moment displays a distinct behavior if nodes in the gap are absent but regions with small, finite, values of the energy gap exist.

72.40.Hi,74.25.Nf,74.20.De

I. INTRODUCTION

In recent years a very significant effort, both experimentally and theoretically, has been made to determine the symmetry of the pairing state[1−5] in high temperature superconductors (HTSC's). It is usually held that such an identification would provide significant clues towards a better understanding of the microscopic mechanism responsible for superconductivity. The symmetry properties of the pairing state itself, being connected to those of the superconducting energy gap, have important physical and technological implications.

There is a large body of experimental results, supported by theoretical work, that is generally interpreted as indicative of a pairing state at least predominantly of the d-wave type[1−3,6], (although there are experiments[7−9] which are difficult to interpret in that framework.) By this, it is meant a pairing state which has an order parameter (OP) which vanishes, or nearly so, along four lines on the Fermi surface (FS). The angle between such lines of nodes (or "quasinodes") is presumed to be near $\pi/2$, but, because of the orthorhombic symmetry of HTSC materials (as exemplified by the strong anisotropy of superconducting properties[10] in the $a-b$ plane) this is unlikely to be precisely correct. Pairing states of different tetragonal symmetry, such as d- or s-wave, could mix. Several proposals, mostly incorporating a predominantly d-wave OP, have been set forth to describe this mixing[11−14]. Some of them include OP's of different symmetry near the surface than in the bulk[15]. Many of the best probes of the OP give information only on the pairing state within a few correlation lengths from the surface, which might differ from the bulk state. Thus, large uncertainties exist.

The aim of this paper is to show that nonlinear electromagnetic phenomena[16−20] can provide a systematic way to distinguish OP's of different symmetries, or of mixed symmetry. We will show how the nonlinear electrodynamic effects in the Meissner regime, which are due to the presence of nodes or small minima in the superconducting gap, can be used to perform "node spectroscopy", that is, to determine the angular position of any lines on the FS where the absolute value of the OP is very small or zero, and the value of the OP at these lines. Further, the bulk character of these effects (they extend over a length on the order of the penetration depth rather than the much smaller coherence length) means that these determinations would refer to the bulk, and can become very useful in avoiding material imperfections near the surface and other difficulties of the surface probes.

We concentrate in this work on the nonlinear magnetic moment as a sensitive probe for the superconducting gap symmetry. In particular, we examine its transverse component (perpendicular to the applied field, which lies in the $a-b$ plane) which is determined by the quasiparticle excitations. Other quantities, such as the penetration depth, might also be used for the same purpose, and will be referred to briefly. The transverse moment, however, can be readily measured either directly or through the torque it produces, and, as shown in Ref. 19, its size for typical samples is large enough to be detected. At temperatures much below the critical temperature, the excitations responsible for the nonlinear Meissner effect are energetically favorable only near the nodes or quasinodes of the FS. The spectroscopy method described in this paper, provides an accurate positioning of the nodes in the energy gap and not just information about their presence. Similarly we show that even in the absence of nodes, the presence of "quasinodes" would lead to several distinctive features in the angular and field dependence of the nonlinear magnetic moment.

We will examine various pairing states that are compatible with the crystal symmetry, including leading candidates for the pairing state of HTSC materials, and excluding only the pure d-wave state which we have extensively discussed elsewhere[19]. In our notation for the pairing states, we shall follow the discussion from Refs. 1,2. We start with the spin singlet pairing states in a square CuO_2 lattice as given in Table I. For the $YBCO$ family of cuprates, the orthorhombic crystal distortion amounts to a simple change in the length of the a and b crystallographic constants. Therefore[1] the admissible mixing of OP's include combinations of $d_{x^2-y^2}$ and s, or of s^- and d_{xy} symmetries only. The nodes of the gap function are not necessarily at an angle $\pi/4$ from the crystallographic axes, and do not in general form an angle of $\pi/2$. For the $BSCCO$ family the situation is different[1,21]. The distortion occurs in such a way that the new orthorhombic axes form an angle of $\pi/4$ with the original tetragonal axes. The relevant mixing is then between d_{xy} and s or between $d_{x^2-y^2}$ and s^- symmetries. The nodes are at the orthorhombic axes and, as in the pure d-wave case, the directions along which they occur form angles of $\pi/2$. In the following sections, we shall use these considerations to choose the gap functions to be studied.

In Section II we discuss methods to solve the nonlinear Maxwell-Equations in the Meissner regime to compute the physical quantities of interest. The general procedure we use exploits the fact, proved in Ref. 19 (see particularly Fig. 5 there) that the angular dependence of the transverse magnetic moment for a typical finite sample (a flat crystal) can be very accurately computed by assuming that the sample is infinite in the $a-b$ plane, while the overall amplitude is underestimated somewhat by this assumption. Since, as we shall see, the nodal structure is directly reflected in the angular dependences, we can proceed for our purposes here by considering a simple "slab" geometry. This allows us to do the entire work analytically, treating the small nonlinear effects perturbatively. We illustrate our perturbation method in Section II by considering first a superconducting gap with mixed $d+s$ symmetry. Various additional gap functions, with nodes, are studied in Section III. We show how to include the effects of orthorhombic distortion as they affect both normal (FS shape) and superconducting (penetration depth tensor) properties, in the calculation of the nonlinear effects. In Section IV we consider gaps without nodes in contrast with the corresponding results obtained in the previous sections. We propose several ways that would allow to experimentally distinguish nodes from small minima in the superconducting gap. In the last Section we give our conclusions and possible guidelines for the future work.

II. METHODS

A. Maxwell-London Electrodynamics

We briefly review here the nonlinear Maxwell-London equations[17–19,22] that need to be solved for superconductors with various pairing states. For a d wave infinite superconductor, these nonlinear equations have been solved, perturbatively[18] at zero temperature, or numerically[17,19] when finite systems or temperatures have been considered.

Here we are concerned with node spectroscopy, that is, with the effect that a pattern of nodes (or deep dips) in the angular dependence of the OP has on the dependence of the nonlinear Meissner effect on the angle between applied field and sample orientation. For this purpose we can work at $T=0$ since it was shown[17] that at the temperatures $T << T_c$ and field ranges experiments are performed, the $T=0$ result is sufficiently accurate. Similarly, we can work in a simple "infinite slab" geometry (as defined below) since it is known[19] that finite size effects, while changing the amplitude of the nonlinear phenomena to some extent, do not affect their angular dependence. We will, therefore, develop a zero temperature perturbation methods, for a simple geometry, that can be used with a wide variety of pairing states. These methods are a nontrivial extension of those used in Ref. 18 for a pure d-wave state.

We consider a superconductor[17,18] infinite in the $a-b$ plane and having a thickness d in the c direction. We will assume unless otherwise stated that d is larger than any relevant penetration depth, (a "slab", not a film). We use a coordinate system with z axis parallel to the c crystallographic direction. We follow the notation introduced in Ref. 19 unless otherwise indicated. The superfluid velocity $\mathbf{v}$ is defined as:

$$\mathbf{v} = \frac{\nabla\chi}{2} + \frac{e}{c}\mathbf{A}, \tag{2.1}$$

where χ is the phase of the superconducting OP, $\mathbf{A}$ the vector potential, and e the proton charge, (with $\hbar = k_B = 1$). The relation between $\mathbf{v}$ and $\mathbf{H}$ is given by the second London equation:

$$\nabla \times \mathbf{v} = \frac{e}{c}\mathbf{H}. \tag{2.2}$$

In the steady state the appropriate Maxwell equation is Ampère's law, $\nabla \times \mathbf{H} = \frac{4\pi}{c}\mathbf{j}$. Combining it with Eq. (2.2) we obtain:

$$\nabla \times \nabla \times \mathbf{v} = \frac{4\pi e}{c^2}\mathbf{j}(\mathbf{v}). \tag{2.3}$$

The relation between $\mathbf{j}$ and $\mathbf{v}$ is generally nonlinear and given by:[18,19]

$$\mathbf{j}(\mathbf{v}) = -eN_f \int_{FS} d^2s\, n(s)\mathbf{v}_f[(\mathbf{v}_f \cdot \mathbf{v}) + 2\int_0^\infty d\xi\, f(E(\xi) + \mathbf{v}_f \cdot \mathbf{v})], \tag{2.4}$$

where N_f is the total density of states at the Fermi level, $n(s)$ the density of states at point s at the Fermi surface (FS), normalized to unity ($\int_{FS} d^2s\, n(s) = 1$), $\mathbf{v}_f(s)$ the s-dependent Fermi velocity, f the Fermi function, with $E(\xi) = (\xi^2 + |\Delta(s)|^2)^{1/2}$, T the absolute temperature and $\Delta(s)$ the OP.

For the geometry considered and for the magnetic field $\mathbf{H}_a$, applied in the $a-b$ plane, the fields have only x and y components, which depend *only* on the coordinate z. Eq. (2.3) then reduces to

$$\partial_{zz}\mathbf{v} + \frac{4\pi e}{c^2}\mathbf{j}(\mathbf{v}) = 0, \tag{2.5}$$

where it is understood that Eq. (2.4) is substituted in the second term. The boundary conditions are:

$$\mathbf{H} = \mathbf{H}_a|_{z=\pm\frac{d}{2}}. \tag{2.6}$$

The first term in (2.4) is the usual relation $\mathbf{j} = -e\tilde{\rho}\mathbf{v}$, where $\tilde{\rho}$ is the superfluid density tensor. At $T = 0$ the nonlinear corrections (in $\mathbf{v}$), described by the second term of Eq. (2.4), and due to the quasiparticle backflow can be written as:

$$\begin{aligned}\mathbf{j}_{qp}(\mathbf{v}) &= -2eN_f \int_{FS} d^2s\, n(s)\mathbf{v}_f\Theta(-\mathbf{v}_f \cdot \mathbf{v} - |\Delta(s)|)[(\mathbf{v}_f \cdot \mathbf{v})^2 - |\Delta(s)|^2]^{1/2} \\ &\approx -2e\sum_n N_{fn} \int_{\Omega_n} \frac{d\phi_n}{2\pi}\mathbf{v}_{fn}[(\mathbf{v}_{fn} \cdot \mathbf{v})^2 - |\Delta(\phi_n)|^2]^{1/2}, \qquad n = 1, 2, ...\end{aligned} \tag{2.7}$$

where we have replaced integration over the whole FS by integration over only the nodal (or quasinodal) regions Ω_n, each region enumerated by the index n, where the gap vanishes (or dips to a value much smaller than its maximum) so that a backflow current due to so called[18] "jets" of quasiparticle excitations is allowed. Quantities at the node n are denoted by an index "n". For an anisotropic FS surface some care has to be taken: at the nodal position s_n, the density of states, $n(s_n)$, is not necessarily equal to the average value, n_{iso}. At each node we therefore define the appropriate weighted density of states $N_{fn} \equiv N_f n(s_n)/n_{iso}$. Regions contributing to the backflow current are determined by

$$|\Delta(\phi_n)| + \mathbf{v}_f \cdot \mathbf{v} < 0, \tag{2.8}$$

where ϕ_n is angle with respect to the closest node, n, in the energy gap, and $\mathbf{v}_f$ can be approximated by $\mathbf{v}_{fn}$, its value at that node. As an example, for a pure d-wave ($d_{x^2-y^2}$) OP, $\Delta(\phi) = \Delta_d \sin(2\phi)$, where ϕ is measured with respect to a node, Eq. (2.7) can be integrated with Ω_n given from Eq. (2.8) by $|\phi_n| \leq \phi_{cn}$, where ϕ_{cn} is determined from:

$$(\mathbf{v}_{fn} \cdot \mathbf{v})^2 = |\Delta_d \sin 2\phi_{cn}| \approx 4\Delta_d^2\phi_{cn}^2, \tag{2.9}$$

and $\phi_{cn} \ll 1$, which implies that the nodal value is an accurate approximation on Ω_n. It follows from these considerations that the nonlinear effects depend on the *local* values of FS quantities at the nodes. The overall shape of the FS enters (as we shall see in more detail below) very indirectly, through the eigenvalues of the London penetration depth tensor.

B. Nonlinear Currents

To perform the calculation of the angular dependence of the nonlinear electrodynamic quantities we must first develop a general method to compute the current, including the nonlinear terms from Eq. (2.7), for the different OP's under consideration. The resulting expressions lead, after substitution into (2.5), to nonlinear differential equations that can be solved perturbatively. It is pedagogically convenient to illustrate both steps by carrying them out in terms of a mixed $d+s$-wave gap function and an isotropic FS. It is then rather straightforward to extend the results to the other forms of the OP and to include the effects of the $a-b$ plane anisotropy.

The specific form of a $d+s$ OP that we consider in this paper is:

$$\Delta_{d+s}(\phi) = \Delta_s + \Delta_d \sin 2\phi, \tag{2.10}$$

where all quantities are real, ϕ is measured from the X axis (Fig. 1), and we take $|\Delta_s| \ll |\Delta_d|$, which ensures that there are nodes in the gap function. The experimental constraints on the smallness of Δ_s/Δ_d have been discussed, for example, by Annett et al.[1,2]. At $\Delta_s = 0$ we will recover the known perturbative results[18] for that limit. The relevance of this form of the gap to YBCO, when the effects of orthorhombicity are taken into account, has been discussed above. For $\Delta_s \neq 0$, the nodes of Eq. (2.10) are no longer separated by an angle of $\pi/2$ since they are shifted by an angle $\pm\nu$ (see Fig. 1),

$$\nu \equiv \frac{1}{2}\sin^{-1}(\frac{\Delta_s}{\Delta_d}), \tag{2.11}$$

from the orthogonal axes, which we denote by X and Y, and which will remain defined throughout the paper as being along the nodal directions of a pure d-wave gap, that is, at angles of $\pi/4$ with the crystallographic axes of YBCO. These axes, together with other details, are shown in Fig. 1. We introduce also nonorthogonal axes along the nodal directions of the $d+s$ gap function with unit vectors $\hat{x}_n$ (n=1,2,3,4 as indicated in the Figure):

$$\hat{x}_1 = -\hat{x}_3 = c\hat{X} - s\hat{Y}, \qquad \hat{x}_2 = -\hat{x}_4 = -s\hat{X} + c\hat{Y}, \tag{2.12}$$

where $c \equiv \cos\nu$ and $s \equiv \sin\nu$. The angles ϕ_n, defined below Eq. (2.8), measure angular shifts from the nodes of Δ_{d+s}, for example, $\phi_1 = \phi + \nu$. Close to the nodal region, the gap has the form:

$$|\Delta_{d+s}(\phi_n)| \approx |\mu\Delta_{eff}\phi_n|, \qquad n = 1, 2, ... \tag{2.13}$$

where the effective amplitude of the gap function $\Delta_{eff} = (\Delta_d^2 - \Delta_s^2)^{1/2}$ is slightly reduced from the pure d-wave limit, and $\mu = 2$ in this case. The allowed region for quasiparticle excitations from Eq. (2.8) is $\phi_n^2 \leq \phi_{cn}^2$ where

$$\phi_{cn}^2 = \frac{(\mathbf{v}_{fn}\cdot\mathbf{v})^2}{\mu^2\Delta_{eff}^2}. \tag{2.14}$$

We will investigate the angular dependence of physical quantities, when the field is applied along different directions with respect to nodes in the gap function. We define, as in Ref. 19, ψ to be the angle of $\mathbf{H}_a$ with the $+\hat{Y}$ direction. This angle is also shown in Fig. 1. From Eqs. (2.7) and (2.8) we see that as ψ changes, various nodes contribute to $\mathbf{j}_{qp}$. Without $a-b$ plane FS anisotropy the integration yields (as a special case from Appendix A):

$$j_{qpi} = \frac{1}{2}eN_f\frac{v_f^3}{\mu\Delta_{eff}}[e_{1i}(\psi)v_X^2 + e_{2i}(\psi)v_Xv_Y + e_{3i}(\psi)v_Y^2], \qquad i = X, Y, \tag{2.15}$$

where the coefficients $e_{1,2,3\,i}(\psi)$ are defined for various ranges of ψ:

$$e_{1X} = e_{3Y} = c^3 - s^3,\ e_{2X} = 2e_{3X} = 2e_{1Y} = e_{2Y} = -2cs(c-s), \quad \psi \in [\nu, \frac{\pi}{2} - \nu] \tag{2.16a}$$

$$e_{1X} = -e_{3Y} = -(c^3 + s^3),\ e_{2X} = -2e_{3X} = 2e_{1Y} = -e_{2Y} = 2cs(c+s), \quad \psi \in [\frac{\pi}{2} - \nu, \pi + \nu]. \tag{2.16b}$$

We can simply verify that for a pure d wave case ($c \equiv 1, s \equiv 0$) these expressions correctly reduce[19] to:

$$j_{qpX,Y} = e\rho_{ab}\frac{v_{X,Y}\,|v_{X,Y}|}{2v_c}, \tag{2.17}$$

where $\rho_{ab} = \frac{1}{2}N_f v_f^2$ is the superfluid density, related to the penetration depth by $\lambda_{ab}^{-2} = \frac{4\pi e^2}{c^2}\rho_{ab}$, and the characteristic velocity in that limit is $v_c \equiv \frac{\Delta_d}{v_f}$. In general, we define

$$v_c \equiv \Delta_{eff}/v_f, \tag{2.18}$$

and a dimensionless velocity

$$u_i \equiv \frac{v_i}{\mu v_c}, \qquad i = X, Y. \tag{2.19}$$

We also define the dimensionless field:

$$h = \frac{H_a}{H_0}, \tag{2.20}$$

where we introduce the characteristic magnetic field as:

$$H_0 = \frac{c\Delta_{eff}}{e\lambda_{ab} v_f}. \tag{2.21}$$

In the case of pure d-wave gap, Eq. (2.21) reduces[19] to $H_0 = \frac{\phi_0}{\pi^2 \lambda_{ab}\xi_{ab}}$, where ϕ_0 is the flux quantum and the in-plane coherence length is defined as $\xi_{ab} = \frac{v_f}{\pi \Delta_d}$. Then, recalling (2.15), we can write (2.5) in dimensionless form as:

$$\partial_{ZZ} u_i - u_i + [e_{1i}(\psi) u_X^2 + e_{2i}(\psi) u_X u_Y + e_{3i}(\psi) u_Y^2] = 0, \qquad i = X, Y. \tag{2.22}$$

Here we have introduced the dimensionless coordinate $Z \equiv z/\lambda_{ab}$, where λ_{ab} is the penetration depth at any of the four equivalent nodes. In the pure d-wave limit the above equations again reduce to the known[18] result. In the geometry considered in this paper j_{qpi} and u_i have definite parity with respect to the Z coordinate and it is sufficient to solve the boundary value problem for half of the slab ($Z \geq 0$). The boundary conditions at the surface $Z = Z_s \equiv \frac{d}{2\lambda_{ab}}$, from Eq. (2.2) are:

$$\partial_Z u_X|_{Z=Z_s} = h\frac{\cos\psi}{\mu}, \qquad \partial_Z u_Y|_{Z=Z_s} = h\frac{\sin\psi}{\mu}, \tag{2.23}$$

and odd parity of $\mathbf{u}$ requires:

$$u_{X,Y} \equiv 0|_{Z=0}. \tag{2.24}$$

C. Perturbation method

In the Meissner regime where $h, u \ll 1$, Eq. (2.22), with the boundary conditions (2.23) and (2.24), can be solved perturbatively. We write $u_i(Z)$ as a sum of linear and quadratic parts in the small[23] parameter h, $u_i(Z) = L_i(Z) + N_i(Z)$. The linear part then satisfies:

$$\partial_{ZZ} L_i(Z) - L_i(Z) = 0, \tag{2.25}$$

with L_i satisfying the boundary conditions (2.23), (2.24). The solution is:

$$L_i(Z) = a_i \sinh(Z), \qquad i = X, Y \tag{2.26}$$

and from Eq. (2.23):

$$a_X = h\frac{\cos\psi}{\mu\cosh(Z_s)}, \qquad a_Y = h\frac{\sin\psi}{\mu\cosh(Z_s)}. \tag{2.27}$$

The nonlinear, perturbation part, in h, N_i, satisfies :

$$\partial_{ZZ} N_i(Z) - N_i(Z) + \bar{a}_i^2 \sinh^2(Z) = 0, \tag{2.28a}$$

$$\bar{a}_i^2 = [e_{1i}(\psi) a_X^2 + e_{2i}(\psi) a_X a_Y + e_{3i}(\psi) a_Y^2], \qquad i = X, Y \tag{2.28b}$$

at $Z = Z_s$ from Eq. (2.23) the boundary conditions are:

$$\partial_Z N_i|_{Z=Z_s} = 0. \tag{2.29}$$

The local magnetic field at $Z = Z_s$ is equal to the applied field. At $Z = 0$, we have from Eq. (2.24) that $N_i(0) \equiv 0$. The complete solution to Eq. (2.28) is a sum of the homogeneous solution, N_{hi} and a particular solution, N_{pi}:

$$N_i(Z) = A_{1i}\sinh(Z) + A_{2i}\cosh(Z) + P_i\cosh(2Z) + R_i \equiv N_{hi}(Z) + N_{pi}(Z), \tag{2.30a}$$

$$A_{1i} = \frac{2}{3}\bar{a}_i^2(\sinh(Z_s) - \tanh(Z_s)),\ \ A_{2i} = -\frac{1}{3}\bar{a}_i^2,\ \ P_i = \frac{1}{3}R_i = -\frac{\bar{a}_i^2}{6}, \qquad i = X, Y. \tag{2.30b}$$

where the coefficients in N_{hi}, A_{1i}, A_{2i}, are obtained using Eq. (2.24) and (2.29). The magnetic field can be calculated from the field $\mathbf{u}$ through Eq. (2.2):

$$H_X(Z) = -H_0[hf_L(Z)\sin\psi + \frac{h^2}{2}(e_{1Y}\cos^2\psi + e_{2Y}\cos\psi\sin\psi + e_{3Y}\sin^2\psi)f_N(Z)], \tag{2.31a}$$

$$H_Y(Z) = +H_0[hf_L(Z)\cos\psi + \frac{h^2}{2}(e_{1X}\cos^2\psi + e_{2X}\cos\psi\sin\psi + e_{3X}\sin^2\psi)f_N(Z)] \tag{2.31b}$$

where

$$\begin{aligned} f_L(Z) &= \frac{\cosh(Z)}{\cosh(Z_s)}, \\ f_N(Z) &= \frac{1}{3\cosh^2(Z_s)}[\,2(\sinh(Z_s) - \tanh(Z_s))\cosh(Z) + 2\sinh(Z) - \sinh(2Z)]. \end{aligned} \tag{2.31c}$$

The above results are valid for any value of d (not just $(d \gg \lambda)$), and we can at once write expressions for measurable quantities. The components of the penetration depth along the two orthogonal directions defined by the axes can be obtained as:

$$\frac{1}{\lambda_X(\mathbf{H}_a)} = \frac{1}{H_a}|\partial_z H_X|_{Z=Z_s}, \qquad \frac{1}{\lambda_Y(\mathbf{H}_a)} = \frac{1}{H_a}|\partial_z H_Y|_{Z=Z_s}. \tag{2.32}$$

For a slab, $Z_s \gg 1$ $(d \gg \lambda)$, a pure d-wave gap function $(\nu = 0)$ and field applied along the node or antinode, one can use these and similar expressions to recover the results for $1/\lambda(\mathbf{H}_a)$ from Refs. 17,18.

We next consider the magnetic moment, in particular its component transverse to the applied magnetic field, which in this case is purely nonlinear for a symmetric sample[24] . In previous work[19,20] we have shown that the magnetic moment (for any sample geometry) can be calculated using only the surface values of the fields. For the geometry considered here, the magnetic moment, defined in general as:

$$\mathbf{m} = \frac{1}{2c}\int d\mathbf{r}\mathbf{r} \times \mathbf{j}(\mathbf{v}), \tag{2.33}$$

can be expressed as:

$$m_{x,y} = -\frac{\mathcal{S}d\,H_{a\,x,y}}{4\pi} \mp \frac{\mathcal{S}c}{2\pi e}v_{y,x}(d/2), \tag{2.34}$$

where x and y are orthogonal axes fixed in space, $\mathcal{S}$ is the slab area, and we have used that $\mathbf{v}$ is odd in z[25]. For a slab, $(d \gg \lambda_{ab})$, which is the case of experimental interest[17], the expressions for $N_{X,Y}$ from Eq. (2.30) simplify:

$$N_i(Z_s) = \frac{h^2}{3\mu^2}(e_{1i}\cos^2\psi + e_{2i}\cos\psi\sin\psi + e_{3i}\sin^2\psi) \qquad i = X, Y \tag{2.35}$$

and we obtain the transverse magnetic moment, $m_\perp = m_X\cos\psi + m_Y\sin\psi$:

$$\begin{aligned} m_\perp(\psi) = \frac{\mathcal{S}\lambda_{ab}}{3\mu^2\pi}\frac{H_a^2}{H_0}[&e_{3X}\sin^3\psi - e_{1Y}\cos^3\psi \\ &+ \cos\psi\sin\psi((e_{1X} - e_{2Y})\cos\psi + (e_{2X} - e_{3Y})\sin\psi)]. \end{aligned} \tag{2.36}$$

The most obvious consequence of the s-wave admixture is that the periodicity of $m_\perp(\psi)$ is no longer strictly $\pi/2$, but π, although the $\pi/2$ Fourier component remains larger for small ν. Writing explicitly $e_{1,2,3\,i}$ we have:

$$m_{\perp}(\psi) = \frac{\mathcal{S}\lambda_{ab}}{12\pi}\frac{H_a^2}{H_0}(c-s)(\cos\psi - \sin\psi)[cs + (1+4cs)\cos\psi\sin\psi], \quad \psi \in [\nu, \frac{\pi}{2} - \nu] \tag{2.37a}$$

$$m_{\perp}(\psi) = -\frac{\mathcal{S}\lambda_{ab}}{12\pi}\frac{H_a^2}{H_0}(c+s)(\cos\psi + \sin\psi)[cs + (1-4cs)\cos\psi\sin\psi], \quad \psi \in [\frac{\pi}{2} - \nu, \pi + \nu]. \tag{2.37b}$$

We can readily extend this solution for $m_{\perp}(\psi)$ to the remaining ψ range by symmetry. In the limit $\nu \rightarrow 0$, corresponding to a pure d-wave, we recover the known result for this limit[26].

The above expressions are in terms of the angle ψ with a line of nodes. In an experimental situation the position of the line of nodes is not *a priori* known, since it depends on the amount of Δ_s admixture, which is to be determined. All one has to do is to plot $m_{\perp}$ as a function of angle, with arbitrary origin, and compare the shape of the curve, up to an horizontal translation, with the plots presented below.

We now show in Fig. 2 the angular dependence of $m_{\perp}(\psi)$ from Eq. (2.37) for $\psi \in [-\frac{\pi}{4}, \frac{3\pi}{4}]$. This interval is a complete period for the plotted quantity. The solid line represents the pure d-wave result, with its maximum normalized to unity. The actual unnormalized value of its amplitude as a function of applied field and sample parameters can be read off Eq. (2.37). It is discussed in detail, with inclusion of finite size effects, in Refs. 19,20, where typical values of H_0, h, $\mathcal{S}$, and other sample parameters, are given. The other lines depict $m_{\perp}(\psi)$ for a $d{+}s$ gap. They are normalized by the same factor as the solid line, so that the relative effects of introducing an s component can be gauged. These curves, which are (see Eq. (2.37)) independent of the applied field, are labeled by the value of the angle ν, the shift of the nodal directions from the d-wave nodes. The relation between ν and Δ_s/Δ_d is given by Eq. (2.11). If we take $\nu < 0$ ($d - s$ gap) the lines are simply shifted by $\pi/2$. In Fig. 2 we see that when the nodal directions are not orthogonal, and hence the period of $m_{\perp}$ doubles from its d-wave value, the formerly equivalent values of the maxima and minima of $|m_{\perp}(\psi)|$ take increasingly different values. One of the maxima becomes now the primary maximum, and its value increases with $|\nu|$, while the value of the other maximum decreases with $|\nu|$. The overall increase in the maximum nonlinear effect occurs largely because the contributions from the two quasiparticle "jets" at each node tend to cancel each other to a lesser extent when the angle between them is larger than $\pi/2$, that is, near the primary maximum. From the symmetry of the $d + s$ gap function, for any ν (and isotropic FS), when the field is applied along antinodes, $\mathbf{v} \parallel \mathbf{j}$ and $m_{\perp}(\psi) \equiv 0$ when $\psi = 2(n+1)\pi/4$, $n = 0, 1, 2, ..$ (for d-wave this is also true for the field applied along the nodes).

For experimental analysis, it may be convenient to examine the main Fourier components of the periodic $m_{\perp}(\psi)$ curve, in particular its part quadratic in the applied field H_a. As one can see from Fig. 2, the transverse moment has odd parity with respect to ψ if the angle is measured from a line of *antinodes*. With that choice, only the coefficients of the sine terms in the Fourier analysis are nonvanishing. The ones corresponding to π and $\pi/2$ periodicities are easily obtained from Eq. (2.37):

$$m_2 = \frac{\mathcal{S}\lambda_{ab}}{3\pi}\frac{H_a^2}{H_0}[cs(1 + \frac{1}{5}\cos 2\nu) + \frac{1}{12}\sin 2\nu - \frac{1}{20}\sin 6\nu], \tag{2.38a}$$

$$m_4 = \frac{\mathcal{S}\lambda_{ab}}{3\pi}\frac{H_a^2}{H_0}[\frac{1}{4} - 2c^2s^2 - \frac{2}{15}\cos 4\nu + \frac{1}{28}\cos 6\nu + \frac{1}{7}cs\sin 6\nu], \tag{2.38b}$$

where m_2 and and m_4 are the π and $\frac{\pi}{2}$ Fourier components of $m_{\perp}(\psi)$, respectively. When Fourier components are computed with respect to an arbitrary angular origin, one will in general measure both sine and cosine coefficients, but the square root of the sum of their squares should equal the absolute value of the results given in Eq. (2.38).

In Fig. 3 we plot the Fourier components m_2, m_4, as a function of ν and at a constant field, normalized so that m_4 is unity for d-wave. The solid line represents m_4. We see that despite the overall period having doubled, this Fourier component is only slightly reduced for the range of ν we consider[2]. The π component, m_2, is depicted by the dotted line and it increases monotonically with ν.

In the following sections we will focus on the nonlinear transverse magnetic moment for different forms of gap functions. Other quantities could be obtained as shown above. We will see that the generalization of the methods discussed in this Section for the evaluation of the currents and for the perturbation values of the fields is straightforward.

III. GAP FUNCTIONS WITH NODES

In this section we consider additional relevant order parameters with nodes. We will include the details of the derivations in so far as they differ from the example discussed above, but the emphasis will be in the results for the angular dependence of the transverse moment.

A. Anisotropic d-wave states

The first examples we consider are those of a pure d-wave order parameter, with nodes at $\pi/2$ angles, but where the FS in the $a-b$ plane is anisotropic, so that the penetration depths are not equivalent. This is a possible state for both the YBCO and BSCCO families. For the latter case the situation is easier since the Fermi velocities at the nodes are still aligned with the X or Y orthogonal axes. We therefore concentrate on the more complicated first case, where the Fermi velocities at the nodes are not aligned with these axes, but are equal in magnitude.

1. YBCO type orthorhombicity

For YBCO, although the orthorhombic distortion of the crystal lattice is small, there is a quite significant in-plane penetration depth anisotropy,[10] ($\lambda_a^2/\lambda_b^2 \sim 2-6$). Even for a pure d-wave gap function, the vectors $\mathbf{v}_{fn}$ no longer lie along the nodal directions $\pm\hat{X}$, $\pm\hat{Y}$, but are shifted by an angle $\pm\nu_A$. We define ν_A as the angle between the $+\hat{Y}$ axis and $\mathbf{v}_{f2}$. In Fig. 4 we show relevant quantities for an anisotropic FS and the more general case of a $d+s$ gap. The pure d-wave limit, considered in this subsection, corresponds to setting $\nu \equiv 0$ in the Figure. We can write ν_A in terms of an anisotropy parameter Λ_0:

$$\nu_A \equiv tan^{-1}(\frac{\Lambda_0^2-1}{\Lambda_0^2+1}), \tag{3.1}$$

where Λ_0 can be evaluated in terms of Fermi surface parameters. For an ellipsoidal FS one has $\Lambda_0 = \frac{\lambda_a}{\lambda_b}$, but our results for the nonlinear currents are not restricted to this case, since they depend only on the properties at the nodes, not on the details of the shape of the FS. Then, $\mathbf{v}_{fn} = v_{fn}\hat{x}_n$ and $v_{f1} \equiv v_{f2} \equiv v_{f3} \equiv v_{f4}$ with the directions given by:

$$\hat{x}_1 = -\hat{x}_3 = \frac{(c_A - s_A)}{\sqrt{2}}\hat{a} - \frac{(c_A + s_A)}{\sqrt{2}}\hat{b}, \quad \hat{x}_2 = -\hat{x}_4 = \frac{(c_A - s_A)}{\sqrt{2}}\hat{a} + \frac{(c_A + s_A)}{\sqrt{2}}\hat{b}, \tag{3.2}$$

where $\hat{a}, \hat{b}$ are unit vectors along the a, b crystallographic axes, $c_A \equiv \cos\nu_A$ and $s_A \equiv \sin\nu_A$. The calculation is then quite analogous to that done in the previous section. We can obtain, from Appendix A, $j_{qp\,i}$ as given in Eq. (2.15) with v_f being replaced by v_{fn}. The linear part is obtained most conveniently in terms of the principal axes of the superfluid density tensor, which in this case are the crystallographic directions. If we now define the dimensionless length Z in terms of λ_n ($\lambda_n^{-2} = \frac{2\pi e^2}{c^2}N_{fn}v_{fn}^2$), the penetration depth at the nodes, (instead of λ_{ab}), $v_c \equiv \frac{\Delta_d}{v_{fn}}$ and $H_0 \equiv \frac{c\Delta_d}{e\lambda_n v_{fn}}$, then by following the steps leading to the derivation of (2.22) and the discussion from Appendix A, we obtain:

$$\partial_{ZZ}u_i - \frac{\lambda_n^2}{\lambda_i^2}u_i + [e_{1i}(\psi)u_a^2 + e_{2i}(\psi)u_a u_b + e_{3i}(\psi)u_b^2] = 0, \qquad i = a,b \tag{3.3}$$

which is formally identical to (2.22) and is solved in the same way. We can express the linear part of the velocity components along the principal axes as:

$$L_i(Z) = a_i \sinh(r_i Z), \qquad i = a,b \tag{3.4a}$$

$$a_a = h\frac{\cos(\psi - \frac{\pi}{4})}{\mu r_a \cosh(r_a Z_s)}, \qquad a_b = h\frac{\sin(\psi - \frac{\pi}{4})}{\mu r_b \cosh(r_b Z_s)}, \tag{3.4b}$$

where we have defined $r_i \equiv \lambda_n/\lambda_i$, $i = a,b$. The nonlinear part satisfies:

$$\partial_{ZZ}N_i - r_i^2 N_i + [e_{1i}a_a^2\sinh^2(r_a Z) + e_{2i}a_a a_b \sinh(r_a Z)\sinh(r_b Z) + e_{3i}a_b^2\sinh^2(r_b Z)], \tag{3.5}$$

with the solution $N_i(Z) \equiv N_{hi}(Z) + N_{pi}(Z)$, where:

$$N_{hi}(Z) = A_{1i}\sinh(r_i Z) + A_{2i}\cosh(r_i Z), \qquad i = a,b \tag{3.6}$$

$$N_{pi}(Z) = P_i\cosh(2r_a Z) + R_i\cosh((r_a + r_b)Z) + S_i\cosh((r_a - r_b)Z) + T_i\cosh(2r_b Z) + U_i. \tag{3.7}$$

After determining the unknown coefficients from the boundary conditions, as explained in Appendix B, we obtain:

$$N_a(Z_s) = \frac{h^2}{12}[e_{1a}\frac{\cos^2(\psi - \frac{\pi}{4})}{r_a^4} + \frac{3e_{2a}\cos(\psi - \frac{\pi}{4})\sin(\psi - \frac{\pi}{4})}{r_a^2 r_b(2r_a + r_b)} + \frac{3e_{3a}\sin^2(\psi - \frac{\pi}{4})}{r_a r_b^2(r_a + 2r_b)}], \tag{3.8a}$$

$$N_b(Z_s) = \frac{h^2}{12}[\frac{3e_{1b}\cos^2(\psi - \frac{\pi}{4})}{r_a^2 r_b(2r_a + r_b)} + \frac{3e_{2b}\cos(\psi - \frac{\pi}{4})\sin(\psi - \frac{\pi}{4})}{r_a r_b^2(r_a + 2r_b)} + \frac{e_{3b}\sin^2(\psi - \frac{\pi}{4})}{r_b^4}]. \tag{3.8b}$$

In addition to the nonlinear transverse magnetic moment, quadratic in H_a, there is a transverse component linear in H_a due to the anisotropy of the FS. From Eq. (2.26) and (2.34) we get for the linear part, $m_\perp^{lin}(\psi)$:

$$m_\perp^{lin}(\psi) = \frac{\mathcal{S}}{4\pi} H_a(\lambda_a - \lambda_b)\cos 2\psi. \tag{3.9}$$

Experimentally, the different angular and, particularly, field dependence should provide a way to separate the effects of $m_\perp^{lin}$ from the quantity of interest, the nonlinear $m_\perp$ which reflects the symmetry of the superconducting gap, rather than that of the normal state. From Eq. (2.34) and (3.8) we can express the nonlinear part of $m_\perp$, as in the $d + s$ case, in terms of the angle ψ:

$$\begin{aligned} m_\perp(\psi) = {} & \frac{\mathcal{S}\lambda_n}{12\pi}\frac{H_a^2}{H_0}(c_A - s_A)(\cos\psi - \sin\psi)\frac{1}{4}[3\frac{(c_A + s_A)^2}{r_a r_b^2(r_a + 2r_b)} - \frac{(c_A - s_A)^2}{r_a^4} \\ & + (18\frac{(c_A + s_A)^2}{r_a r_b^2(r_a + 2r_b)} - 2\frac{(c_A - s_A)^2}{r_a^4})\cos\psi\sin\psi], \qquad \psi \in [\psi_1, -\psi_1 + \frac{\pi}{4}] \end{aligned} \tag{3.10a}$$

$$\begin{aligned} m_\perp(\psi) = {} & -\frac{\mathcal{S}\lambda_n}{12\pi}\frac{H_a^2}{H_0}(c_A + s_A)(\cos\psi + \sin\psi)\frac{1}{4}[3\frac{(c_A - s_A)^2}{r_a^2 r_b(2r_a + r_b)} - \frac{(c_A + s_A)^2}{r_b^4} \\ & - (18\frac{(c_A - s_A)^2}{r_a^2 r_b(2r_a + r_b)} - 2\frac{(c_A + s_A)^2}{r_b^4})\cos\psi\sin\psi], \qquad \psi \in [-\psi_1 + \frac{\pi}{4}, \psi_1 + \pi]. \end{aligned} \tag{3.10b}$$

where $\tan(\psi_1 - \frac{\pi}{4}) = \frac{\lambda_b}{\lambda_a}\tan(\frac{\pi}{4} + \nu_A)$, as explained in Appendix B. The effect of FS anisotropy on $m_\perp(\psi)$ is similar to that due to the presence of an s-wave gap, discussed in the previous section. The period is doubled from the pure d-wave and isotropic FS value. The results from Eq. (3.10) can be simply extended to include an admixture of s-wave gap and we will defer their discussion for the following subsection.

2. BSCCO type orthorhombicity

Here we consider the nonlinear current response for a d-wave OP when there is a FS anisotropy consistent with the orthorhombicity of materials in the BSCCO family. The effects of the orthorhombic distortion relevant to the OP symmetry are discussed in Refs. 1,2, and in the Introduction. The nodal lines of the $d_{x^2-y^2}$ gap functions are along the X, Y axes. These axes are now the principal orthorhombic directions. As a consequence, the Fermi speeds at the nodes are nonidentical ($v_{fX} \neq v_{fY}$) and the nonlinear current which is generically $\propto v_{fn}^3$ will differ along the X, Y directions. Hence, some small changes are needed in the procedure used for the YBCO case. We define the unit of length in terms of $\lambda \equiv \sqrt{\lambda_{nX}\lambda_{nY}}$, where λ_{ni}, $i = X, Y$ is defined analogous to λ_n, given above Eq. (3.3). We introduce λ and $v_f \equiv \sqrt{v_{fX}v_{fY}}$, in the previous definitions of the dimensionless units, for example, in $Z \equiv z/\lambda$ and in H_0 from Eq. (2.21). We define $q_i \equiv (\lambda/\lambda_i)^{1/2}$, $i = X, Y$ and obtain:

$$\begin{gathered} \partial_{ZZ}u_i - q_i^2 u_i + p_i^2[e_{1i}(\psi)u_X^2 + e_{2i}(\psi)u_X u_Y + e_{3i}(\psi)u_Y^2] = 0, \\ p_i^2 \equiv q_i^2\frac{\lambda_i^2}{\lambda_{ni}^2}\frac{v_{fi}}{v_f}, \qquad i = X, Y \end{gathered} \tag{3.11}$$

where the only nonvanishing coefficients $e_{1,2,3,i}$ are (cf. Eq. (2.17)), $e_{1X} = e_{3Y} = 1$ for $\psi \in [0, \pi/2]$ and $-e_{1X} = e_{3Y} = 1$ for $\psi \in [\pi/2, \pi]$. The part of the velocity linear in h, L_i, has the form given by Eq. (3.4) with r_i replaced by q_i and $\psi - \frac{\pi}{4}$ by ψ. The nonlinear part in h, N_i, from Eq. (3.11) satisfies :

$$\partial_{ZZ}N_i(Z) - q_i^2 N_i(Z) + \bar{a}_i^2\sinh^2(q_i Z) = 0, \qquad i = X, Y \tag{3.12a}$$

$$\bar{a}_X^2 = p_X^2 e_{1X} a_X^2, \qquad \bar{a}_Y^2 = p_Y^2 e_{3Y} a_Y^2, \tag{3.12b}$$

It is straightforward, following the $YBCO$ case, to write the complete solution for N_i and obtain for a slab:

$$N_X(Z_s) = \frac{h^2}{12}\frac{p_X^2}{q_X^2} e_{1X}\cos^2\psi, \qquad N_Y(Z_s) = \frac{h^2}{12}\frac{p_Y^2}{q_Y^2} e_{3Y}\sin^2\psi. \tag{3.13}$$

The corresponding nonlinear transverse magnetic moment is

$$m_\perp(\psi) = \frac{\mathcal{S}\lambda}{12\pi}\frac{H_a^2}{H_0}\cos\psi\sin\psi[e_{1X}\frac{p_X^2}{q_X^2}\cos\psi - e_{3Y}\frac{p_Y^2}{q_Y^2}\sin\psi], \tag{3.14}$$

where e_{1X} and e_{3Y} are as given below Eq. (3.12). We see that the two terms, which correspond to two "jets" of quasiparticle backflow excitations in the nodal directions are of different strengths since $p_X/q_X \neq p_Y/q_Y$. We illustrate this effect on the angular dependence of $m_\perp$ in Fig. 5. We use here the same conventions as in Fig. 2. The solid line represents results obtained for $m_\perp(\psi)$ in the isotropic FS case, with its maximum normalized to unity. They should be contrasted with the broken line which corresponds to results with $\lambda_Y/\lambda_X = 1.1$,[27] normalized by the same factor. We have used Ref. 28 to estimate $\lambda_i/\lambda_{ni} \sim \sqrt{2}$, and set $v_{fX}/v_{fY} = \lambda_Y/\lambda_X = 1.1$. Half a period for $m_\perp$ is shown, the plot can be extended by odd parity over the whole range, $\psi \in [-\pi/2, \pi/2]$. The behavior of $m_\perp$ is somewhat similar to that for a $d+s$ gap and isotropic FS (Fig. 2), but instead of $m_\perp$ vanishing for a field applied along the antinodes it vanishes here when the field is applied along the nodal directions.

B. Anisotropic d+s

The derivation of (3.10) can be combined with that of (2.37) to include an s-wave component in the energy gap, i.e. $\Delta_{d+s}(\phi)$ from Eq. (2.10), in the presence of FS anisotropy of the YBCO type. Examination of the derivations of the equations just mentioned shows that the crucial point about the additional s term is that the shifts in the direction of the $\mathbf{v}_{fn}$ from the $\pm\hat{X}$, $\pm\hat{Y}$ axes, arising from the anisotropy and from the s component must be combined. Thus the total shift angle ν_A, introduced in Fig. 4, must include the effect of ν as well as that of Λ_0^2. For an ellipsoidal FS this is achieved by replacing Λ_0^2 in Eq. (3.1) with:

$$\Lambda^2 = \Lambda_0^2\tan(\frac{\pi}{4} + \nu), \tag{3.15}$$

and we note that if ν is small and $\Lambda_0^2 \approx 1$ then $\nu_A \approx \nu_A^0 + \nu$, where ν_A^0 is the contribution arising solely from FS anisotropy. With these generalizations, the results for $m_\perp(\psi)$ in terms of ν_A are still given by Eq. (3.10). Some care has to be taken with redefining dimensionless quantities. The characteristic velocity is taken to be $v_c = (\Delta_d^2 - \Delta_s^2)^{1/2}/v_{fn}$.

In Fig. 6 we show the results from Eq. (3.10) for the nonlinear transverse magnetic moment $m_\perp(\psi)$ (the linear part is given by Eq. (3.9)). In the Figure, we give results for $\Lambda_0 \equiv \lambda_a/\lambda_b = 1.5$ (which is in the correct range[10] for YBCO) and take $\lambda_n^2 = \lambda_a\lambda_b$. Again, the solid line is our standard reference result: pure d-wave and isotropic FS, normalized to unity. The broken lines are labeled by their ν_A values and are normalized by the same factor. For the value of Λ_0 employed, the range of ν_A that we have chosen to display would correspond, for an ellipsoidal FS, to slightly negative values of ν. This seems physically appropriate to describe YBCO, where the chains are in the b direction and $\lambda_a > \lambda_b$. The departure of $m_\perp(\psi)$ from $\pi/2$ periodicity can be very significant when the effects of ν and ν_A^0 are in the same direction. The precise shape of $m_\perp(\psi)$ is the result of the combined effects of FS anisotropy, reflected in the penetration depth, and of the s wave contribution. Experimental results for $m_\perp(\psi)$ would yield ν_A, and information about the FS (i.e., Λ_0) would be needed to infer ν.

C. Extended s-wave states

The results we have discussed so far were obtained for nodes along four directions on the FS. It is straightforward to include symmetries of the OP with a larger number of nodes, as we have already mentioned in the derivation leading to (2.7). Among the allowed spin singlet pairing states[1] of a single CuO_2 plane with square lattice structure that have not been considered yet, are the A_{2g} or "g-wave", and the "extended s-wave" states, with eight nodes.[29] The gap function for the former case can be written as

$$\Delta_{es}(\phi) = \Delta_s + \Delta_g \sin 4\phi, \tag{3.16}$$

where $|\Delta_s| \ll |\Delta_g|$. The g-wave is the limit $\Delta_s \equiv 0$. We have used an angle ϕ measured from the g-wave nodal direction, along the $+X$ axis (more conventionally, for an angle measured from the a-axis, the sine in Eq. (3.16) would have been replaced by a cosine, and reflect the same symmetry properties[1] of Δ_{es} and the simple s-wave gap for a square lattice). The differences between pure g-wave and extended s-wave, written in this form, are similar to those between d and $d+s$ gap functions as explored in Section II. For example, the nodes are shifted from the g-wave gap by an angle $\pm\nu$, where we have:

$$\nu \equiv \frac{1}{4}\sin^{-1}(\frac{\Delta_s}{\Delta_g}), \tag{3.17}$$

and ν is the angle between the direction of closest node to the $+X$ axis and the $+X$ axis. The gap function at the nodes can be approximated by

$$|\Delta_{es}(\phi_n)| \approx \left|4(\Delta_g^2 - \Delta_s^2)^{1/2}\phi_n\right|, \tag{3.18}$$

with ϕ_n taken with the respect to the node n of $\Delta_{es}(\phi)$. If we take an isotropic FS, the Fermi velocity at the nodal directions is given by $v_{fn}\hat{x}_n$ with

$$\begin{aligned} \hat{x}_1 &= -\hat{x}_5 = c\hat{X} - s\hat{Y},\ \ \hat{x}_2 = -\hat{x}_6 = c_\alpha\hat{X} + s_\alpha\hat{Y}, \\ \hat{x}_3 &= -\hat{x}_7 = s\hat{X} + c\hat{Y},\ \ \hat{x}_4 = -\hat{x}_8 = -s_\alpha\hat{X} + c_\alpha\hat{Y}, \end{aligned} \tag{3.19}$$

where $c \equiv \cos\nu$, $s \equiv \sin\nu$, $c_\alpha \equiv \cos\alpha$, $s_\alpha \equiv \sin\alpha$, and $\alpha \equiv \pi/4 + \nu$.

After obtaining the nonlinear current by performing the sum in (2.7) over all eight nodes, the solution for the velocity field is readily found as in the $d+s$ case, noting that now $\mu \equiv 4$ and the coefficients $e_{1,2,3\,i}$ are different. The period of $m_\perp(\psi)$ becomes $\pi/2$. The nonlinear current is of the form (2.15) with

$$\begin{aligned} e_{1X} &= c^3 - s^3 + c_\alpha^3 + s_\alpha^3,\ \ e_{2X} = 2(-cs^2 - c^2 s + c_\alpha^2 s_\alpha - c_\alpha s_\alpha^2) = 2e_{1Y}, \\ e_{3X} &= cs^2 - c^2 s + c_\alpha^2 s_\alpha + c_\alpha s_\alpha^2 = \frac{1}{2}e_{2Y},\ \ e_{3Y} = -c^3 - s^3 - c_\alpha^3 + s_\alpha^3, \qquad \psi \in [\nu, \frac{\pi}{4} - \nu] \end{aligned} \tag{3.20a}$$

$$\begin{aligned} e_{1X} &= c^3 + s^3 + c_\alpha^3 + s_\alpha^3,\ \ e_{2X} = 2(cs^2 - c^2 s + c_\alpha^2 s_\alpha - c_\alpha s_\alpha^2) = 2e_{1Y}, \\ e_{3X} &= cs^2 + c^2 s + c_\alpha^2 s_\alpha + c_\alpha s_\alpha^2 = \frac{1}{2}e_{2Y},\ \ e_{3Y} = c^3 - s^3 - c_\alpha^3 + s_\alpha^3, \qquad \psi \in [\frac{\pi}{4} - \nu, \frac{\pi}{2} + \nu]. \end{aligned} \tag{3.20b}$$

With the aid of Eq. (2.36) we can obtain the corresponding $m_\perp(\psi)$:

$$\begin{aligned} m_\perp(\psi) = \frac{\mathcal{S}\lambda_{ab}}{48\pi}\frac{H_a^2}{H_0}&[(c+s)(cs - \frac{s}{\sqrt{2}}(c-s))\cos^3\psi + (s-c)(cs - \frac{c}{\sqrt{2}}(c+s))\sin^3\psi \\ &+ \cos\psi\sin\psi[((c-s)(1+3cs) + \sqrt{2}c(1 - \frac{3}{2}(c^2 - s^2)))\cos\psi \\ &+ ((c+s)(1-3cs) - \sqrt{2}s(1 + \frac{3}{2}(c^2 - s^2)))\sin\psi]], \qquad \psi \in [\nu, \frac{\pi}{4} - \nu] \end{aligned} \tag{3.21a}$$

$$\begin{aligned} m_\perp(\psi) = \frac{\mathcal{S}\lambda_{ab}}{48\pi}\frac{H_a^2}{H_0}&[(c-s)(cs + \frac{s}{\sqrt{2}}(c+s))\cos^3\psi + (c+s)(cs + \frac{c}{\sqrt{2}}(c-s))\sin^3\psi \\ &+ \cos\psi\sin\psi[((c+s)(1-3cs) + \sqrt{2}c(1 - \frac{3}{2}(c^2 - s^2)))\cos\psi \\ &- ((c-s)(1+3cs) + \sqrt{2}s(1 + \frac{3}{2}(c^2 - s^2)))\sin\psi]], \qquad \psi \in [\frac{\pi}{4} - \nu, \frac{\pi}{2} + \nu] \end{aligned} \tag{3.21b}$$

where in the first definition of H_0, in Eq. (2.21), we have replaced Δ_{eff} by $(\Delta_g^2 - \Delta_s^2)^{1/2}$.

D. Mixed d+g Gap Functions

Mixed pairing states compatible with the presence of orthorhombic distortion also include[1,2] $d+g$-wave states, i.e., "$s^- + d_{xy}$" for the *YBCO* family and "$s^- + d_{x^2-y^2}$" for *BSCCO*. We consider here only the first case with an isotropic FS. The other cases can be treated similarly. We again assume that the d-wave character is dominant and we denote the gap function we use, with $\Delta_d \gg \Delta_g$:

$$\Delta_{d+g}(\varphi) = \Delta_d \sin 2\varphi + \Delta_g \sin 4\varphi, \tag{3.22}$$

where φ is measured from the a axis. At the four nodes we can approximate the absolute value of the gap function, needed to calculate j_{qp}, with :

$$|\Delta_{d+g}(\phi_n)| \approx |2(\Delta_d \pm 2\Delta_g)\phi_n| \,. \tag{3.23}$$

We have again contributions from two inequivalent quasiparticle "jets", in this case due to the different values of the gap near the nodes. The solution for the linear part of the velocity is the same as for the pure d-wave, discussed in the previous Section. If we define $u_i \equiv v_i/2v_c$, $v_c \equiv \Delta_d/v_f$ the nonlinear part of velocity satisfies:

$$\partial_{ZZ}N_i(Z) - N_i(Z) + \bar{a}_i^2 \sinh^2(Z) = 0, \qquad i = X, Y \tag{3.24a}$$

$$\bar{a}_X^2 = \frac{1}{1+2r} e_{1X} a_X^2, \qquad \bar{a}_Y^2 = \frac{1}{1-2r} e_{3Y} a_Y^2, \tag{3.24b}$$

where $r \equiv \Delta_s/\Delta_d$, and a_X, a_Y are given by Eq. (2.27). The solution of Eq. (3.24) for a slab is readily obtained as:

$$N_X(Z_s) = \frac{h^2}{12}\frac{e_{1X}}{(1-2r)}\cos^2\psi, \qquad N_Y(Z_s) = \frac{h^2}{12}\frac{e_{3Y}}{(1+2r)}\sin^2\psi. \tag{3.25}$$

The corresponding transverse magnetic moment is

$$m_\perp(\psi) = \frac{\mathcal{S}\lambda}{12\pi}\frac{H_a^2}{H_0}\cos\psi\sin\psi\left[\frac{e_{1X}}{1+2r}\cos\psi - \frac{e_{3Y}}{1-2r}\sin\psi\right], \tag{3.26}$$

where e_{1X}, e_{3Y} are given from Eq. (2.17). This result is formally similar to that for an anisotropic d-wave for BSCCO, recall Eq. (3.14) and Fig. 5, with the substitutions $p_X^2/q_X^2 = 1/(1+2r)$ and $p_Y^2/q_Y^2 = 1/(1-2r)$. For brevity, we have not included plots in this and the previous subsections, but the interested reader can easily generate them from the analytic forms (3.21) and (3.26).

IV. NODELESS GAP FUNCTIONS

In this section we discuss the nonlinear supercurrent response when there are strictly speaking no nodes but there are regions ("quasinodes") with a very small although finite superconducting gap. For an example of a nodeless gap function of this type we choose $s + id$[30,31] pairing. This is a frequently considered candidate for a gap function without nodes, and it clearly illustrates the difference in the nonlinear response when the nodes are absent and only small minima in the gap function exist. The range of $|\Delta_s/\Delta_d|$ that we consider is restricted to the very small values compatible with the bounds set by experiment[2]. For these values, the quasiparticle contribution is dominated by the behavior at the "quasinodes" and the general procedures presented in the previous sections can be used. We will again concentrate here on the nonlinear magnetic moment, as a probe to identify the symmetry of the gap function. The behavior of $m_\perp$ for the $s + id$ state is similar to that which would occur for some other gap functions, such as an "anisotropic s-wave", proposed in the framework of interlayer tunneling by Chakravarty et al.,[32] or for $d_{x^2-y^2} + id_{xy}$[33].

For brevity, we will assume an isotropic FS (equivalent nodes). Anisotropy can be added using the methodology of the previous section. We consider an $s + id$ gap function of the form $\Delta_{s+id}(\phi) = \Delta_s + i\Delta_d \sin(2\phi)$, with $\Delta_s \ll \Delta_d$, where ϕ is the angle with respect to the $+X$ axis, which is still minimum of $|\Delta_{s+id}(\phi)|$. The phase space available for quasiparticle excitations is reduced compared to the d-wave case so that the critical angle (recall Eq. (2.8)) is:

$$\phi_{cn}^2 = \frac{(\mathbf{v}_f \cdot \mathbf{v})^2 - \Delta_s^2}{4\Delta_d^2}, \tag{4.1}$$

There are no nonlinear effects present if $v < v_T \equiv \Delta_s/v_f$ or correspondingly if H_a is smaller than a threshold field h_T which we shall see is $h_T \equiv \Delta_s/\Delta_d$. We can again perform an approximate integration of Eq. (2.4) and obtain an equation for the velocity field ($\psi \in [0, \frac{\pi}{2}]$):

$$\partial_{ZZ}u_i - u_i + (u_i^2 - u_T^2)\Theta(u_i - u_T) = 0, \qquad i = X, Y \tag{4.2}$$

where $u_i = \frac{v_i}{2v_c}$, v_c is as defined for the d wave state, and $u_T \equiv \frac{\Delta_s}{2\Delta_d}$. The step function Θ arises from the nonlinear effects being present only for sufficiently large fields.

We proceed with the perturbation calculation as previously developed, noting that we have to treat carefully the nonanalyticity associated with the step function[34] in Eq. (4.2). To do so, we divide the $Z \geq 0$ portion of the slab (the solution for negative Z follows from the symmetry) into two regions, the first where $u_i \geq u_T$ or correspondingly $Z \in [Z_{Ti}, Z_S]$ and the second for $u_i < u_T$, that is, for $Z \in [0, Z_{Ti})$, where the position Z_{Ti} is to be determined. The solution for the linear part $L_i(Z)$ is the same as in the d-wave case. For the nonlinear part $N_i(Z)$ we have from (4.2):

$$\partial_{ZZ}N_i - N_i + L_i^2 - u_T^2 = 0, \qquad Z \in [Z_{Ti}, Z_S] \qquad i = X, Y \tag{4.3a}$$

$$\partial_{ZZ}N_i - N_i = 0, \qquad Z \in [0, Z_{Ti}) \qquad i = X, Y. \tag{4.3b}$$

$N_i(Z \leq Z_T)$ can then be expressed in the form of Eq. (2.25) and for $Z \leq Z_T$ we can write:

$$N_i(Z) = A_{3i}\sinh(Z), \qquad i = X, Y \tag{4.4}$$

where we have used $N_i(0) = 0$. After finding the coefficients P_i and R_i in the particular solution for $Z \geq Z_T$, we are left with four unknown parameters A_{1i}, A_{2i}, A_{3i} and the matching point Z_{Ti}. They are determined from Eq. (2.29) and by requiring continuity of velocity, magnetic field, and current at $Z \equiv Z_{Ti}$. One has the same number of conditions and of unknowns. Straightforward algebra yields:

$$\begin{aligned} A_{1i} = & -\frac{a_i^2}{6}[\tanh(Z_s)\cosh(Z_{Ti})(1 - 2\sinh^2(Z_{Ti})) - 4\sinh(Z_s)] \\ & -(\frac{a_i^2}{2} + u_T^2)\tanh(Z_S)\cosh(Z_{Ti}), \end{aligned} \tag{4.5a}$$

$$A_{2i} = \frac{a_i^2}{6}\cosh(Z_{Ti})(1 - 2\sinh^2(Z_{Ti})) + (\frac{a_i^2}{2} + u_T^2)\cosh(Z_{Ti}), \tag{4.5b}$$

$$\begin{aligned} A_{3i} = & -\frac{a_i^2}{6}[\tanh(Z_s)\cosh(Z_{Ti})(1 - 2\sinh^2(Z_{Ti})) - 4\sinh(Z_s) \\ & + \sinh(Z_{Ti})(1 + 2\cosh^2(Z_{Ti}))] + (\frac{a_i^2}{2} + u_T^2)[\sinh(Z_{Ti}) - \tanh(Z_S)\cosh(Z_{Ti})], \end{aligned} \tag{4.5c}$$

$$P_i = -\frac{a_i^2}{6}, \qquad R_i = -\frac{a_i^2}{2} - u_T^2, \qquad \sinh(Z_{Ti}(\psi)) = \frac{u_T}{a_i(\psi)}, \qquad i = X, Y \tag{4.5d}$$

where in the last expression we have emphasized the angular dependence of the matching point Z_{Ti}. From these equations we obtain that $N_i(Z_s = Z_{Ti}) = 0$. For the slab, when $Z_s \gg 1$, the expression for $N_i(Z_s)$ is simply:

$$N_x(Z_s) = [\frac{1}{12}h^2\cos^2\psi - u_T^2 + \frac{4u_T^3}{3h\cos\psi}]\Theta(h - \frac{\Delta_s}{\cos\psi\Delta_d}), \tag{4.6a}$$

$$N_y(Z_s) = [\frac{1}{12}h^2\sin^2\psi - u_T^2 + \frac{4u_T^3}{3h\sin\psi}]\Theta(h - \frac{\Delta_s}{\sin\psi\Delta_d}). \tag{4.6b}$$

We see from these expressions that for very small fields $h < h_T$, with $h_T \equiv \Delta_s/\Delta_d$ the nonlinear effects vanish. For each jet of quasiparticles to be excited the applied field has to be $h \geq h_{Ti}(\psi)$, where $h_{Ti}(\psi)$ are angle dependent threshold fields, the minimum value of which is the overall threshold field h_T. If we now compute $\mathbf{m}_\perp$ as in the derivation of Eq. (2.36), we find:

$$
\begin{aligned}
m_\perp(\psi) = \frac{\mathcal{S}\lambda_{ab}}{12\pi}\,&[\frac{H_a^2}{H_0}\cos\psi\sin\psi[\cos\psi\Theta(h-h_{TX}) - \sin\psi\Theta(h-h_{TY})] \\
&+ 3(\frac{\Delta_s}{\Delta_d})^2 H_0[\cos\psi\Theta(h-h_{TY}) - \sin\psi\Theta(h-h_{TX})] \\
&- 2(\frac{\Delta_s}{\Delta_d})^3\frac{H_0^2}{H_a}[\cot\psi\Theta(h-h_{TY}) - \tan\psi\Theta(h-h_{TX})]],
\end{aligned} \tag{4.7}
$$

where h_{TX} and h_{TY} are the threshold fields along the X and Y directions respectively, which can be read off Eq. (4.6). It is apparent from this result that in this case $m_\perp$ has a more complicated angular and field dependence than in the d-wave gap (the limit $u_T \equiv \frac{\Delta_s}{2\Delta_d} \to 0$ corresponds to the pure d-wave), or indeed than in any of the other cases considered in the previous sections. In contrast to what occurs with gap functions with nodes, where the applied field dependence is simply given by an overall factor of H_a^2, the angular and applied magnetic field dependences of $m_\perp$ are now coupled, with the coupling depending on the ratio Δ_s/Δ_d. This coupling can best be described by noticing the scaling property of the transverse moment at any angle, which follows from Eq. (4.7):

$$
m_\perp(\kappa h, \kappa\frac{\Delta_s}{\Delta_d}) = \kappa^2 m_\perp(h, \frac{\Delta_s}{\Delta_d}), \tag{4.8}
$$

where κ is a scaling factor.

In Fig. 7 we show our results for the angular dependence of $m_\perp$ at two values of the dimensionless field, $h = 0.05$ and $h = 0.1$. We plot $m_\perp(\psi)$ in the range $\psi \in [0, \pi/4]$ and this can be extended from the odd parity, $m_\perp(\pi/4+\psi) = -m_\perp(\pi/4-\psi)$, to the range of its period, $\pi/2$. The solid curve represents the d-wave result, such that its maximum at field $h = 0.05$ is normalized to unity. As in our discussion of Fig. 2, we refer the reader to previous work[19], for the unnormalized values of this quantity. The broken lines represent $m_\perp(\psi)$ for various Δ_s/Δ_d values, and attain their maxima at different angles ψ_M. The range of Δ_s/Δ_d included is greater than that allowed by experiment, so that the scaling (with $\kappa = 2$) given by Eq. (4.8) can be illustrated. The threshold effect is already evident in this Figure. The nonlinear effects are suppressed for very small applied fields, but recover quickly and indeed the maximum value of the plotted quantity is slightly enhanced at larger fields. This slight enhancement arises in part from the same reasons as in the $d+s$ case, discussed above. Although the "*is*" component leads to a reduction in the phase space available, this reduction is made up for, at larger fields, by the suppression of whichever one of the two "jets" is below the angular dependent threshold, so that the region where the contributions of the two nodes tend to cancel is diminished. In Eq. (4.7), for d wave, we see that for $0 < \psi < \pi/2$ both jets contribute. In that limit (from the first line in Eq. (4.7)) the contributions of two jets have opposite signs, partially cancelling each other. With the addition of a small s-wave component there are two trends: first there is a small reduction in the phase space available for the quasiparticle jets, resulting in smaller contributions of individual jets, but also there will be a region where cancelation of the two jets will be reduced.

We show next in Fig. 8 , the variation with applied field of the maximum value of the transverse moment a as a function of angle, for various values of Δ_s/Δ_d. There are several interesting features in this Figure. The field dependence is no longer $\propto h^2$, except for the $\Delta_s \to 0$ limit (pure d-wave, depicted by the solid line). The broken lines (corresponding to several values of Δ_s/Δ_d as in the previous Figure) display the existence of the threshold field h_T. The value of h_T can be clearly seen from the Figure to be Δ_s/Δ_d, as given above. There is also, as previously discussed, a region of parameter space $h, \Delta_s/\Delta_d$, with a slightly enhanced $m_{\perp,max}$ compared to the d-wave case.

V. CONCLUSIONS

We have shown in this paper how, at low temperature, the nonlinear magnetic moment can serve as a high quality bulk probe to do "node spectroscopy" in HTSC's, that is, to investigate the position of the nodes (or quasinodes) in pairing states with possible mixed symmetries. We have obtained analytic results for $m_\perp(\psi)$ and a variety of pairing states. Analytic results are possible because the low temperature nonlinear response due to quasiparticle excitations depends on the local properties of the FS and of the energy gap near the nodes. We have examined these effects on $m_\perp$ comparing them to previous results[18,19] for a pure d-wave and isotropic FS. For gaps with nodes, $m_\perp$ is $\propto H_a^2$ and we have concentrated on the angular dependence of $m_\perp(\psi)$.

In sections II and III, we have shown that even a small (real) admixture of an s component to the dominant d-wave OP, would be detectable in $m_\perp(\psi)$. We have found that $m_\perp(\psi)$ is closely linked to the direction of $\mathbf{v}_f$ at the nodes (quasinodes) in the energy gap. Even for an isotropic FS, the directions of the $\mathbf{v}_f$ at the nodes are no longer mutually orthogonal: the nodes become inequivalent and the period of $m_\perp(\psi)$ doubles to π. Experimentally, as can be seen from Fig. 3, it may still be convenient to examine the $\pi/2$ and π Fourier components of $m_\perp(\psi)$ to determine the admixture of s-wave. We also have studied the effect of the $a-b$ plane penetration depth anisotropy on the pure d-wave state. If experimental values as reported for YBCO[10] are used, such an anisotropy significantly alters the corresponding d-wave result with an isotropic FS. We have included the influence of orthorhombic distortion on $m_\perp(\psi)$, for both the YBCO and BSCCO families of cuprates. These effects can be understood in terms of an angle ν_A reflecting the combined effects of an anisotropic FS and the admixture of s component.

In Section IV we have investigated gap functions with quasinodes. The concrete example of an $s+id$ gap clearly shows that $m_\perp$ is a very sensitive probe that allows one to distinguish nodes from quasinodes. To do so, one must consider both its angular and field dependences. The angular dependence is no longer independent of the applied field, and the field dependence is not $\propto H_a^2$. There is a characteristic threshold field $H_T = H_0\Delta_s/\Delta_d$ required to create quasiparticles. No nonlinear effects are present for $H_a < H_T$. These distinct features of $m_\perp(\psi)$ strongly suggest that they are generic to the other forms of gap function with quasinodes.

We have focused here on clean superconductors. This is because, as shown in the extensive discussion of Refs. 17,18, impurities are unimportant, for clean available samples, except at very small applied fields. The methods that we have described in this paper can be readily extended to other forms of gap functions, such as those that attribute an explicit role to the presence of chains[35] in YBCO-like cuprates, or to other combinations not included here.

Possible future extensions of this work also include incorporating an explicit time dependence of the applied field, since the use of more sensitive experimental AC techniques to measure the nonlinear effects is contemplated.[36]

ACKNOWLEDGMENTS

We thank A. Bhattacharya and A. M. Goldman for many useful conversations related to the experimental work on the nonlinear magnetic moment. We also thank J. A. Sauls and B. P. Stojković for discussions.

APPENDIX A: CURRENTS

We give here the general analytic expression for $\mathbf{j}_{qp}(\mathbf{v})$ at low temperature. For a superconducting gap that can be approximated at the node n by $|\Delta(\phi_n)| \approx |\mu\Delta_{eff,n}\phi_n|$, $n=1,2,...$, elementary integration of Eq. (2.7) yields:

$$\begin{aligned}\mathbf{j}_{qp}(\mathbf{v}) &\approx -2e\sum_n N_{fn}v_{fn}\hat{x}_n\mu\Delta_{eff,n}\int_{-\phi_{cn}}^{\phi_{cn}}\frac{d\phi_n}{2\pi}[\phi_{cn}^2-\phi_n^2]^{1/2} \\ &= -\frac{e}{2}\sum_n N_{fn}\hat{x}_n v_{fn}^3\frac{(\mathbf{v}\cdot\hat{x}_n)^2}{\mu\Delta_{eff,n}}, \qquad n=1,2,...\end{aligned} \tag{A1}$$

where for various directions of the applied field, summation will be over different nodes and ϕ_{cn} is given by Eq. (2.14). For YBCO, including the effect of FS anisotropy, we set $\Delta_{eff,n} = \Delta_{eff}$ (see section III), and obtain that nodes 3, 4 contribute to $\mathbf{j}_{qp\,a,b}$ if $\psi \in [\psi_1, \psi_2]$. At $\psi = \psi_1$ only node 3 contributes to the quasiparticle excitations, therefore the expressions for $\mathbf{j}_{qp\,a,b}$ from Eq. (A1) with summation over nodes 2, 3 and over nodes 3, 4 should coincide. Writing explicitly $\mathbf{j}_{qp\,a}$, quadratic in h, in dimensionless form we have:

$$e_{1a}(\psi)L_a^2(Z) + e_{3a}(\psi)L_b^2(Z) = e_{2b}(\psi)L_a(Z)L_b(Z), \qquad \psi = \psi_1 \tag{A2}$$

which gives (we recall Eq. (3.4)):

$$\tan(\psi_1(Z) - \frac{\pi}{4}) \equiv -\frac{\lambda_b}{\lambda_a}\tan(\frac{\pi}{4}+\nu_A)\frac{\tanh(r_a Z)}{\tanh(r_b Z)}. \tag{A3}$$

Unlike in the case of an isotropic FS, the angular range of the applied field contributing to certain nodes is a function of Z. For a slab we can simplify various expressions by taking $\psi_1(Z) \sim \psi_1(Z_s) \equiv \psi_1$, and this was done in Eq. (3.10). In an analogous way we obtain that $\psi_2(Z) = -\psi_1(Z)$ as well as the range for ψ where other nodes contribute. This approximation produces a very small discontinuity in the results at the end points of the intervals in Eq. 2.37. This has been interpolated over in Fig. 6.

APPENDIX B: NONLINEAR VELOCITY FOR AN ANISOTROPIC FS

After evaluating $\mathbf{j}_{qp}$, as discussed in Appendix A, we can cast Eq. (2.5) in dimensionless form. From the perturbation method the nonlinear part in velocity, $\mathbf{N}$, satisfies Eq. (3.5), which is valid for any ψ. The coefficients in Eqs. (3.6) and (3.7) are:

$$\begin{aligned}
A_{1i} &= -A_{2i}\tanh(r_i Z_s) - \frac{2r_a}{r_i}P_i\frac{\sinh(2r_a Z_s)}{\cosh(r_i Z_s)} - \frac{r_a+r_b}{r_i}R_i\frac{\sinh((r_a+r_b)Z_s)}{\cosh(r_i Z_s)} \\
&- \frac{r_a-r_b}{r_i}S_i\frac{\sinh((r_a-r_b)Z_s)}{\cosh(r_i Z_s)} - \frac{2r_b}{r_i}T_i\frac{\sinh(2r_b Z_s)}{\cosh(r_i Z_s)}, \\
A_{2i} &= -P_i - S_i - T_i - U_i, \qquad i = a, b
\end{aligned} \tag{B1a}$$

$$P_a = -\frac{h^2 e_{1a}}{\mu^2 6 r_a^4}\frac{\cos^2\omega}{\cosh^2(r_a Z_s)}, \qquad P_b = -\frac{h^2 e_{1b}}{\mu^2 2 r_a^2(4r_a^2 - r_b^2)}\frac{\cos^2\omega}{\cosh^2(r_a Z_s)}, \tag{B1b}$$

$$\begin{aligned}
R_a &= -\frac{h^2 e_{2a}}{\mu^2 2 r_a 2 r_b^2(2r_a + r_b)}\frac{\cos\omega\sin\omega}{\cosh(r_a Z_s)\cosh(r_b Z_s)}, \\
R_b &= -\frac{h^2 e_{2b}}{\mu^2 2 r_a^2 r_b(r_a + 2r_b)}\frac{\cos\omega\sin\omega}{\cosh(r_a Z_s)\cosh(r_b Z_s)},
\end{aligned} \tag{B1c}$$

$$\begin{aligned}
S_a &= -\frac{h^2 e_{2a}}{\mu^2 2 r_a r_b^2(2r_a - r_b)}\frac{\cos\omega\sin\omega}{\cosh(r_a Z_s)\cosh(r_b Z_s)}, \\
S_b &= \frac{h^2 e_{2b}}{\mu^2 2 r_a^2 r_b(r_a - 2r_b)}\frac{\cos\omega\sin\omega}{\cosh(r_a Z_s)\cosh(r_b Z_s)},
\end{aligned} \tag{B1d}$$

$$T_a = -\frac{h^2 e_{3a}}{\mu^2 2 r_b^2(4r_b^2 - r_a^2)}\frac{\sin^2\omega}{\cosh^2(r_b Z_s)}, \qquad T_b = -\frac{h^2 e_{3b}}{\mu^2 6 r_b^4}\frac{\sin^2\omega}{\cosh^2(r_b Z_s)}, \tag{B1e}$$

$$\begin{aligned}
U_a &= -\frac{h^2}{\mu^2 2 r_a^2}\left(\frac{e_{1a}\cos^2\omega}{r_a^2\cosh^2(r_a Z_s)} + \frac{e_{3a}\sin^2\omega}{r_b^2\cosh^2(r_b Z_s)}\right), \\
U_b &= -\frac{h^2}{\mu^2 2 r_b^2}\left(\frac{e_{1b}\cos^2\omega}{r_a^2\cosh^2(r_a Z_s)} + \frac{e_{3a}\sin^2\omega}{r_b^2\cosh^2(r_b Z_s)}\right),
\end{aligned} \tag{B1f}$$

where $\omega \equiv \psi - \frac{\pi}{4}$ and the coefficients $e_{i,\,1,2,3}$ can be obtained as in the isotropic case.

---

* Electronic address: izutic@physics.spa.umn.edu

[1] J.F. Annett, N. Goldenfeld, and A.J. Leggett, *Physical properties of High Temperature Superconductors V*, D.M. Ginsberg (Ed.), (World Scientific, Singapore, 1996).

[2] J.F. Annett, N. Goldenfeld, and A. J. Leggett, J. Low Temp. Phys. **105**, 473 (1996).

[3] D.J. Scalapino, Phys. Repts. **250**, 331 (1995).

[4] J.R. Kirtley, *et al.*, Nature **373**, 225 (1995).

[5] R.C. Dynes, Sol. State Comm. **92**, 53 (1994). J.R. Schrieffer, Sol. State Comm. **92**, 129 (1994). D. Pines, Physica C, **235-240**, 113, (1994).

[6] H. Aubin, *et al.*, Phys. Rev. Lett. **78**, 2624, (1997).

[7] A.G. Sun, D.A. Gajewski, M.B. Maple and R.C. Dynes, Phys. Rev. Lett. **72**, 2267, (1994).

[8] P. Chaudhari and S.Y. Lin, Phys. Rev. Lett. **72**, 1084, (1994).

[9] J. Buan *et al.*, Phys. Rev. B **54**, 7462 (1996).

[10] D.N. Basov *et al.*, Phys. Rev. Lett. **74**, 598, (1995). K. Zhang *et al.*, Phys. Rev. Lett. **73**, 2484, (1994).
[11] K.A. Müller, Nature **377**, 133 (1995).
[12] H. Kim and E.J. Nicol, Phys. Rev. B **52**, 13576 (1995).
[13] O.T. Valls and M.T. Béal-Monod, Phys.Rev. B **51**, 8438 (1995).
[14] M.T. Béal-Monod and K. Maki, Phys. Rev. B **53**, 5775 (1996).
[15] S.R. Bahcall, Phys. Rev. Lett. **76**, 3634, (1996).
[16] S.K. Yip and J.A. Sauls, Phys. Rev. Lett. **69**, 2264, (1992).
[17] B.P. Stojković and O.T. Valls, Phys. Rev. B **51**, 6049, (1995).
[18] D. Xu, S.K. Yip and J.A. Sauls, Phys Rev. B **51**, 16233, (1995).
[19] I. Žutić and O.T. Valls, Phys. Rev. B **54**, 15500 (1996).
[20] I. Žutić and O.T. Valls, to appear in J. Comput. Phys.
[21] See, e.g., N.M. Plakida, *High Temperature Superconductivity* (Springer, Berlin, 1995), p. 99.
[22] F. London, *Superfluids*, (Wiley, New York, 1950), Vol. 1.
[23] We recall that the applied field H_a must not exceed the field of first flux entry.
[24] That is, e.g., for a disc shaped sample. Otherwise, the linear correction arising from the demagnetization tensor is easily included.
[25] One has to take some care in accounting for all factors of two in the slab geometry: see e.g. E.H. Brandt Phys. Rev. Lett. **76**, 4030, (1994) and Phys. Rev. Lett. **71**, 2821, (1993).
[26] Specifically Eq. (2.21) from Ref. 18. Our definition of H_0 differs from the one in that work by a factor of three.
[27] D.B. Tanner, *et al.*, J. Supercond. **8**, 563 (1995).
[28] M. Oda, *et al.*, Phys. Rev. B **53**, 2253 (1996).
[29] In some cases, the "extended s-wave" gap could have a multiple of eight nodes (see Ref. 3).
[30] G. Kotliar, Phys. Rev. B **37**, 3664 (1988).
[31] Q.P. Li, B.E. Koltenbach and R. Joynt, Phys. Rev. B **48**, 437 (1993).
[32] S. Chakravarty, A. Sudbø, P.W. Anderson and S. Strong, Science **261**, 337 (1993).
[33] M. Sigrist, D.B. Railey and R.B. Laughlin Phys. Rev. Lett. **74**, 3249, (1995)
[34] See, e.g., R.F. Collins, *Mathematical Methods for Physicists and Engineers* (Reinhold, New York, 1968), p. 307.
[35] C. O'Donovan and J.P. Carbotte, Phys. Rev. **B55**, 1200, (1997).
[36] A. Bhattacharya private communication.

FIG. 1. Coordinates and definitions for the $d+s$ OP calculations. The FS and the energy gap are shown schematically. The axes a and b are along the crystallographic directions. The orthogonal X and Y axes are along the nodal directions of the pure d-wave gap. The $d+s$ nodal directions, labeled 1,2,3,4 are shifted by an angle $\pm\nu$ (see Eq. (2.11)) from their $\Delta_s = 0$ values. The applied magnetic field, $\mathbf{H}_a$, forms an angle ψ with the $+Y$ direction.

FIG. 2. Effect of an s component on the angular dependence of the nonlinear transverse magnetic moment. The quantity plotted is $m_\perp(\psi)$, calculated for a $d+s$ gap and an isotropic FS, at constant field, normalized so that its maximum is unity for the pure d-wave (solid line). The broken lines are labeled by the corresponding values of the quantity ν as defined in Eq. (2.11). A full period is shown.

FIG. 3. Fourier components for the case shown in Fig. 2. The results shown are the $\pi/2$ Fourier component (solid line) and the π (broken line) component, at a constant field, as a function of angle ν (Eq. (2.11)). Normalization is taken so that the $\pi/2$ component is unity for a pure d-wave ($\nu = 0$).

FIG. 4. Definitions of various quantities for an anisotropic FS with YBCO type orthorhombicity. The axes a, b, and X, Y, as well as the angles ν and ψ, are defined as in Fig. 1. For clarity, only one node (node 2 in the scheme of Fig. 1) is shown here and the OP is not depicted. The angle ν_A (at the node shown) is the angle between $+\hat{Y}$ and $\mathbf{v}_{f2}$. It has the same magnitude at the other three nodes. The vector $\mathbf{V}$ is the superfluid velocity.

FIG. 5. Angular dependence of $m_\perp(\psi)$, for a pure d-wave OP and a FS with BSCCO type orthorhombicity . The quantities plotted are normalized as in Fig. 2. The solid line represents the isotropic case, and the dashed line the anisotropic case with $\lambda_Y/\lambda_X = 1.1$.

FIG. 6. Angular dependence of $m_\perp(\psi)$, for a $d+s$ OP and YBCO type orthorhombicity. The solid line is the normalized reference result (pure d-wave gap and an isotropic FS). The broken lines, each labeled by the corresponding value of the angle ν_A (see text and Fig. 4) are all obtained for $\lambda_a/\lambda_b = 1.5$.

FIG. 7. Angular dependence of $m_\perp(\psi)$, for various admixtures of s-wave component in an $s+id$ energy gap. Results are shown for two values of the dimensionless field, h=0.05 (panel (a)) and h=0.1 (panel (b)). The normalization is taken so that the pure d-wave (solid line) maximum is unity at h=0.05. The broken lines, are labeled by the corresponding ratio of Δ_s/Δ_d. The scaling property (with $\kappa = 2$) from Eq. (4.8), can be verified by comparing the results for h=0.05 and those for h=0.1 with the appropriate ratios Δ_s/Δ_d increased by a factor of two.

FIG. 8. Field dependence of the maximum of $m_\perp(\psi)$ for various ratios of Δ_s/Δ_d in an $s+id$ state. The solid line is the pure d-wave result normalized so that its value is unity for h=0.05. The broken lines corresponds to the same values of Δ_s/Δ_d as in Fig. 7b. For each value of Δ_s/Δ_d the threshold field $h_T = \Delta_s/\Delta_d$ can be read off from the graph. Except for $\Delta_s \equiv 0$, the lines are not parabolic.

TABLE I. Spin singlet pairing states in a CuO_2 plane.

Symmetry Class	Informal name	Representative State
A_{1g}	s (s^+)	*const.*
A_{2g}	g (s^-)	$xy(x^2-y^2)$
B_{1g}	$d_{x^2-y^2}$	x^2-y^2
B_{2g}	d_{xy}	xy

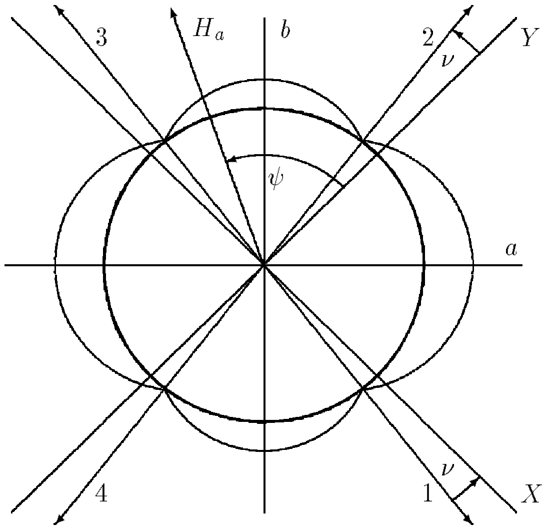

Fig. 1: I. Zutic and O.T. Valls, Gap Spectroscopy

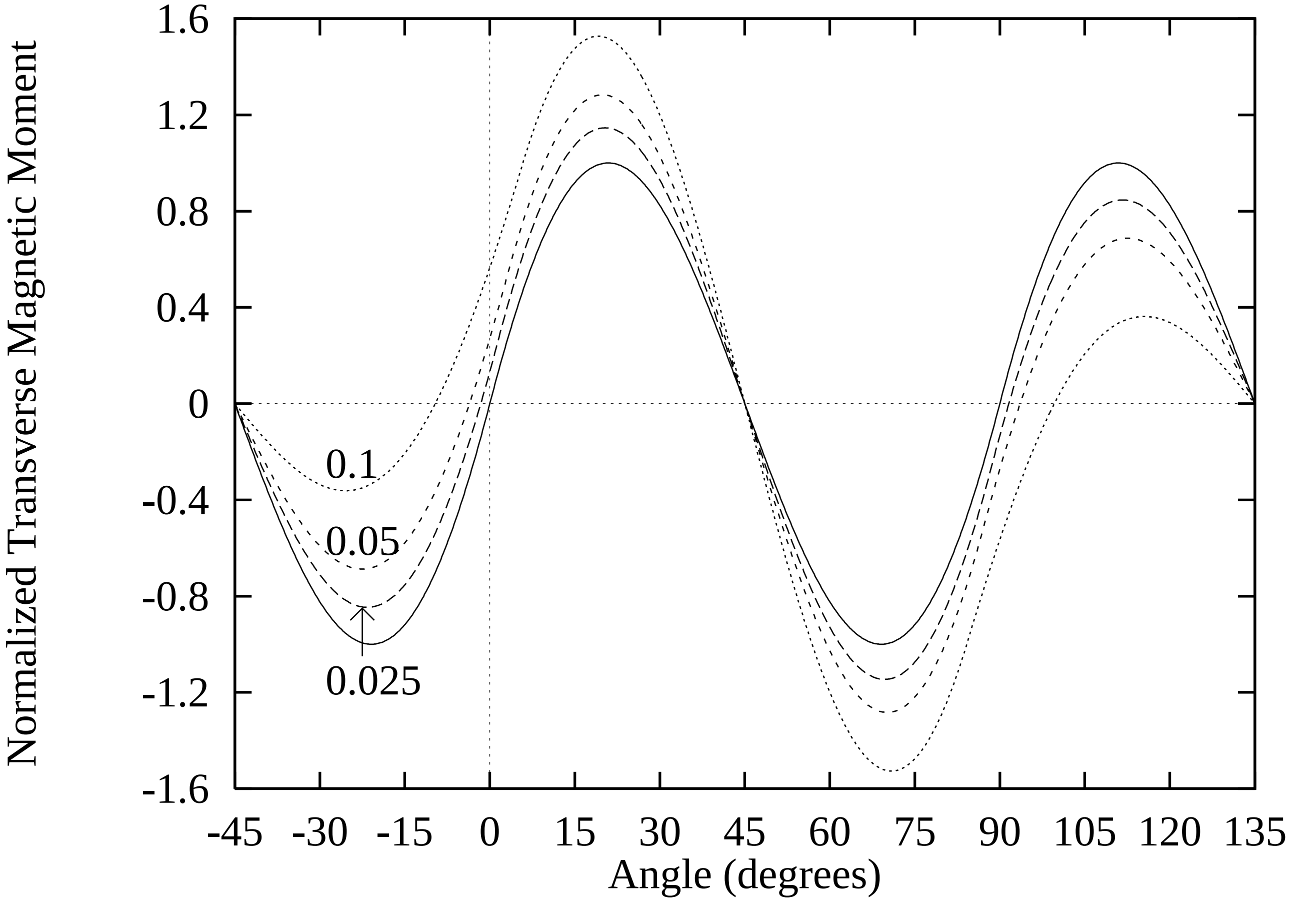

Fig.2: I. Zutic and O.T. Valls, Gap Spectroscopy

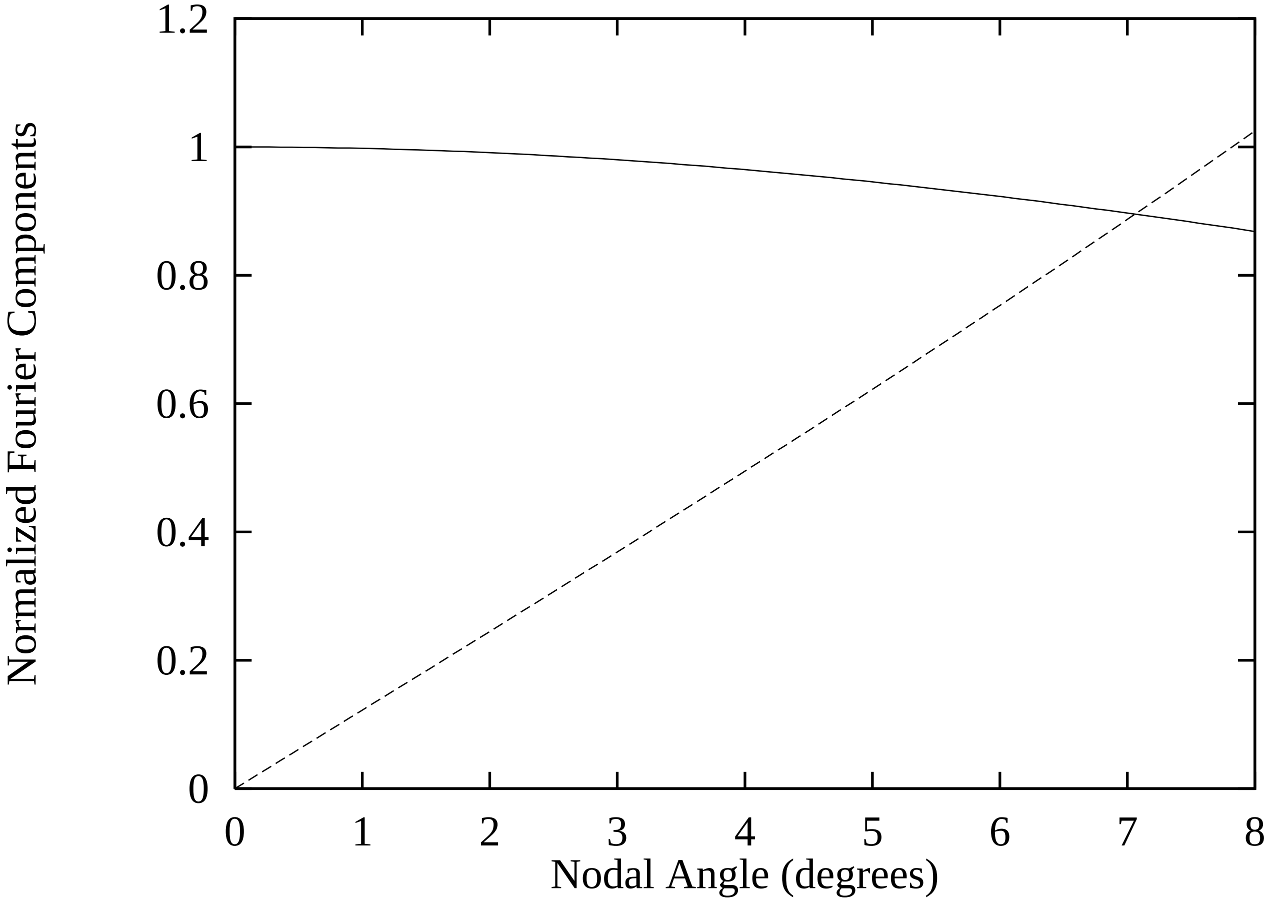

Fig.3: I. Zutic and O.T. Valls, Gap Spectroscopy

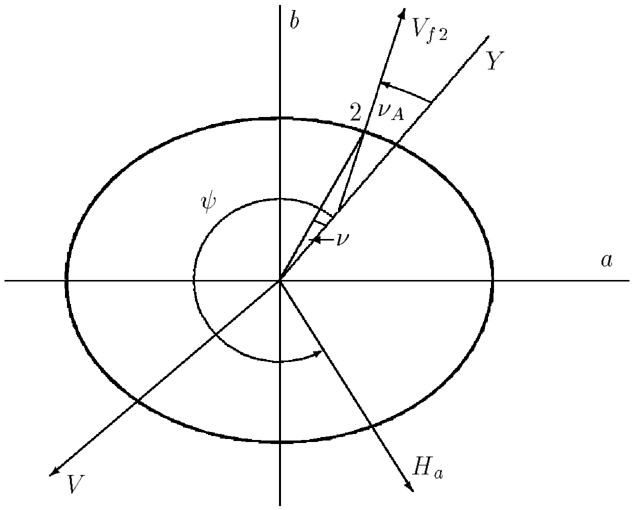

Fig. 4: I. Zutic and O.T. Valls, Gap Spectroscopy

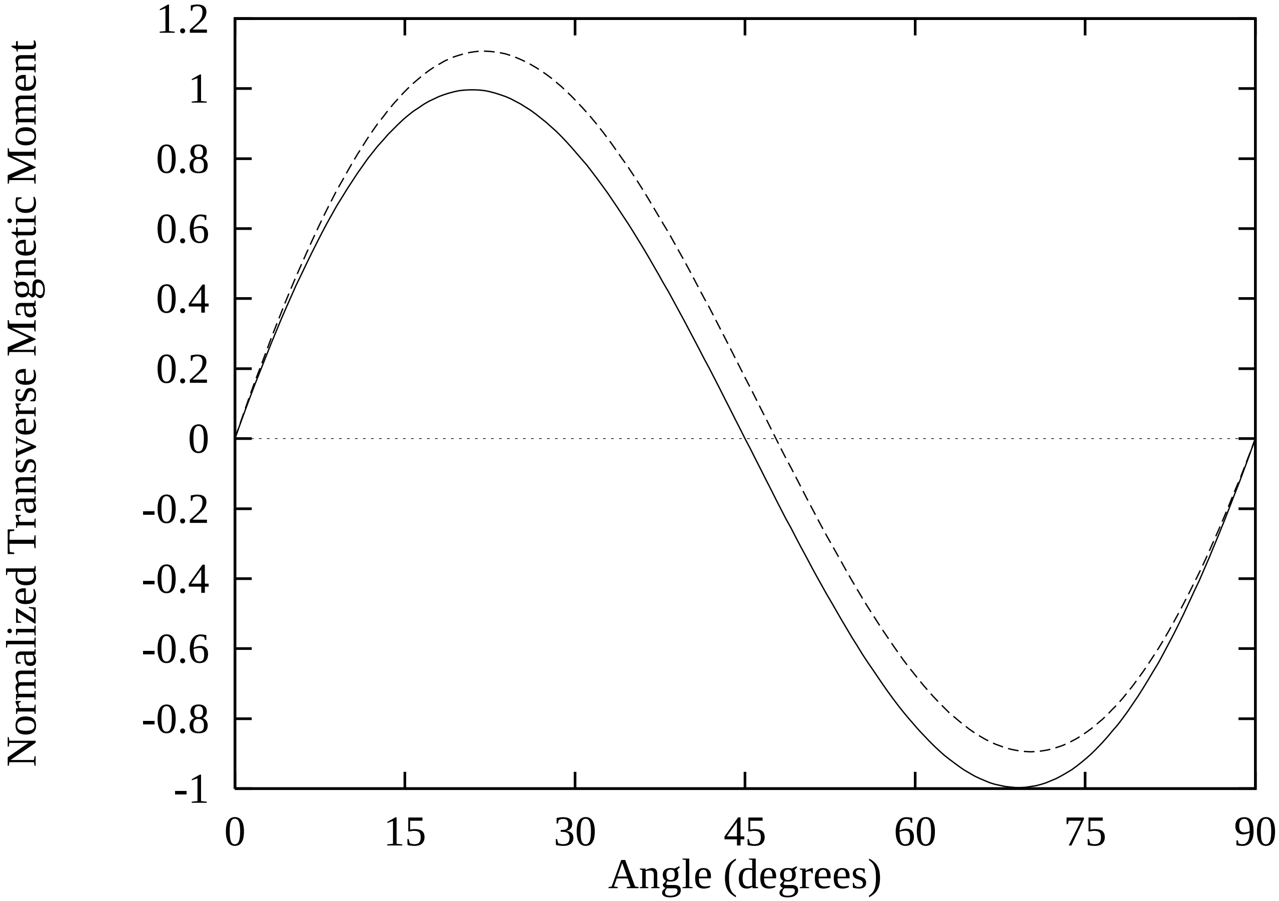

Fig.5: I. Zutic and O.T. Valls, Gap Spectroscopy

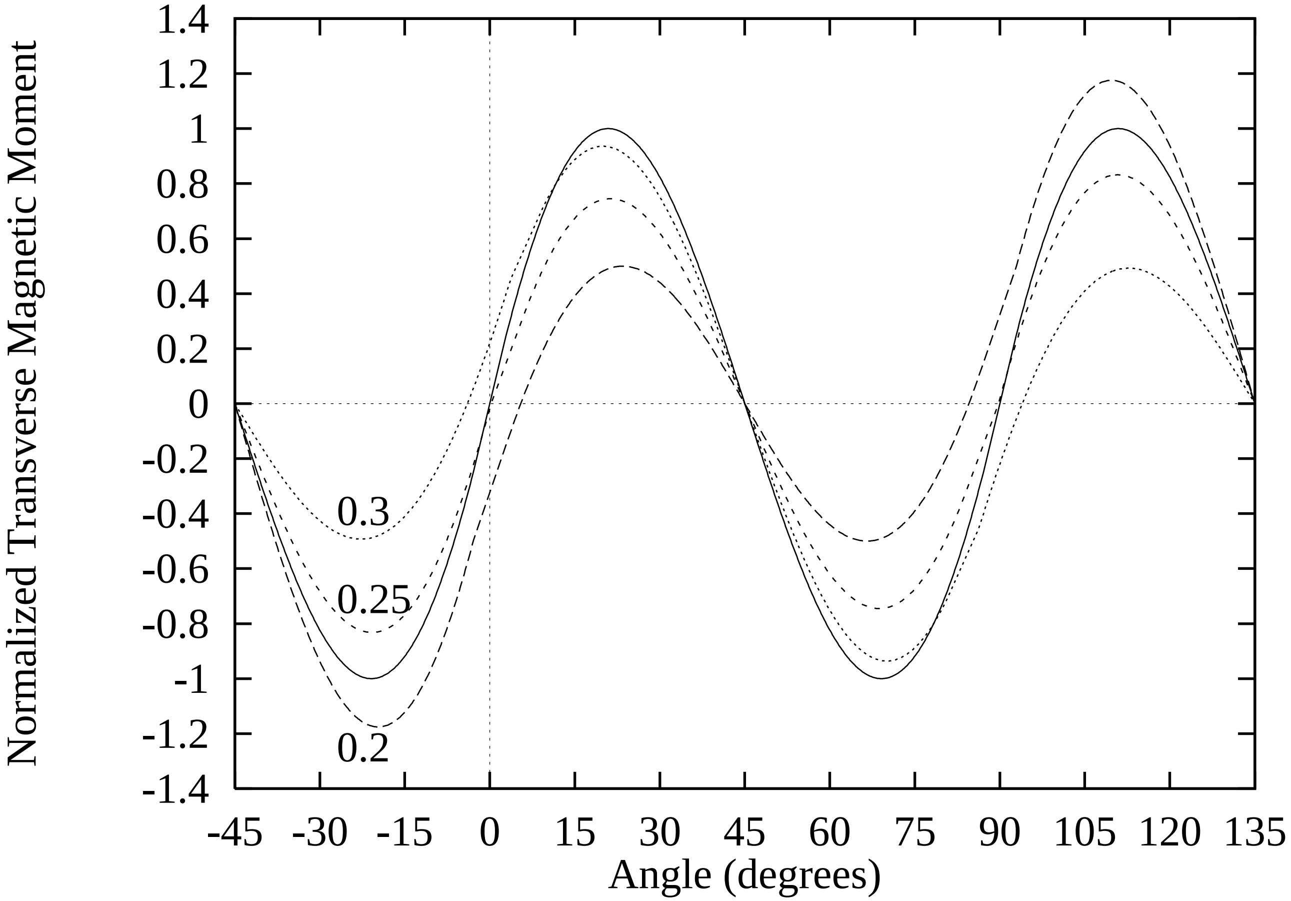

Fig.6: I. Zutic and O.T. Valls, Gap Spectroscopy

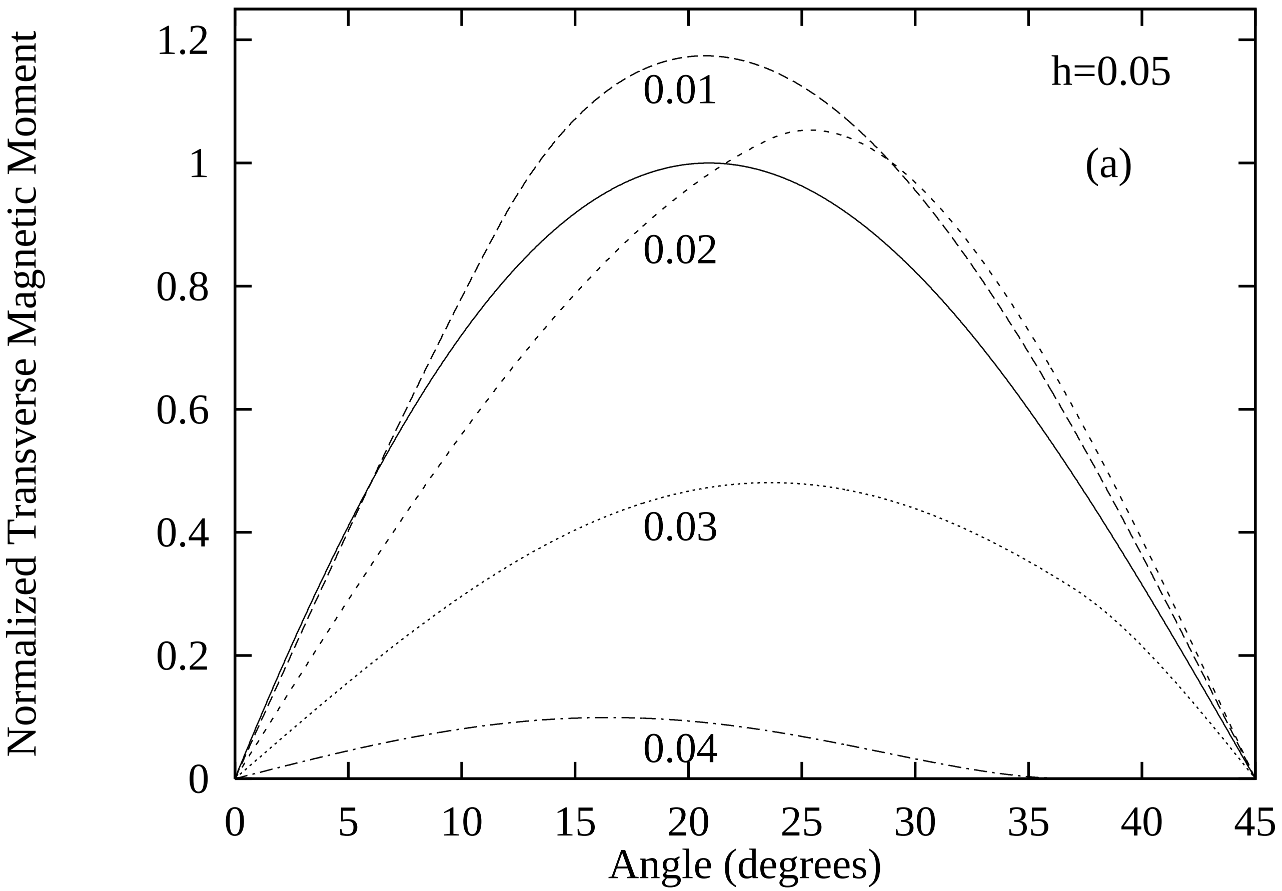

Fig.7a: I. Zutic and O.T. Valls, Gap Spectroscopy

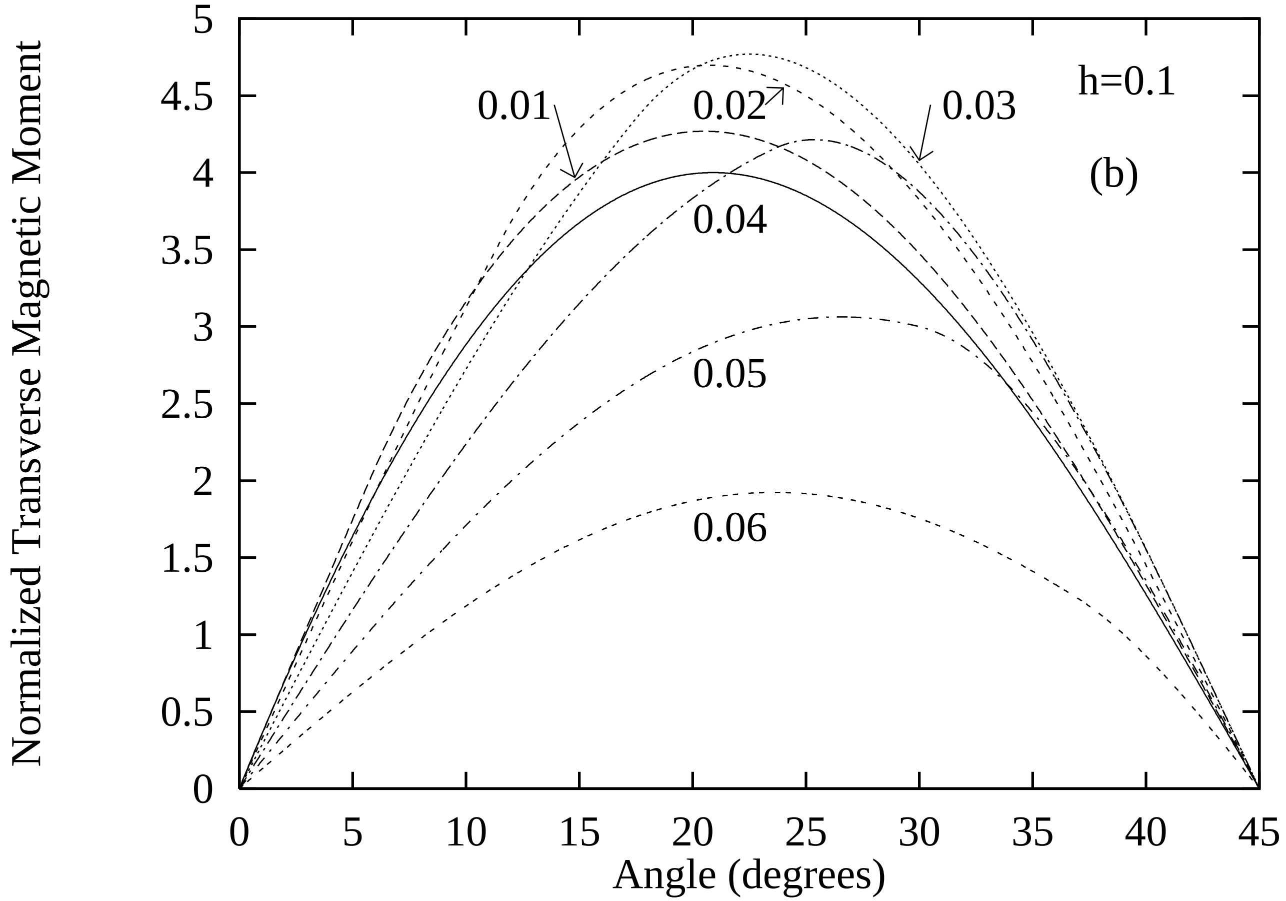

Fig.7b: I. Zutic and O.T. Valls, Gap Spectroscopy

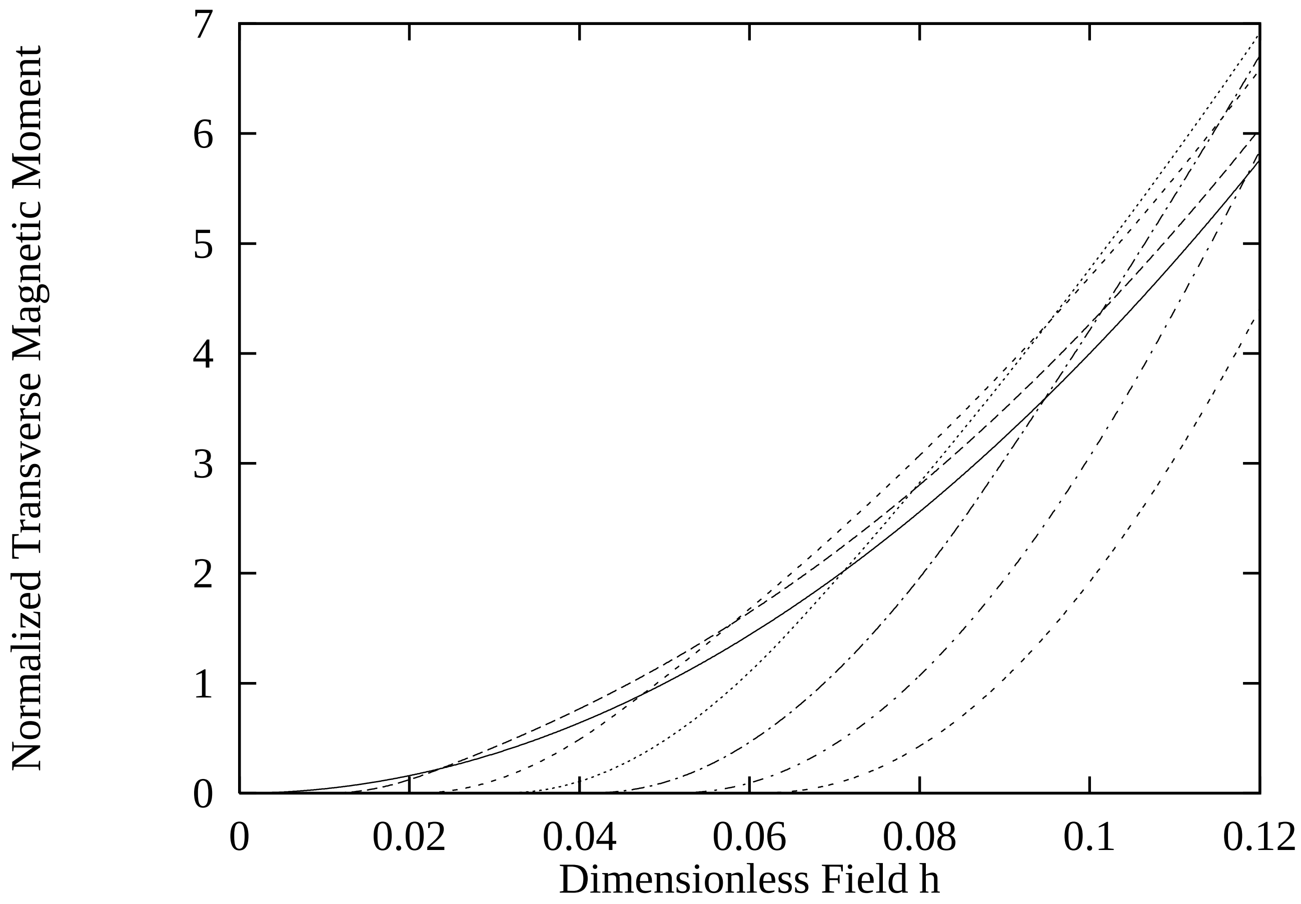

Fig.8: I. Zutic and O.T. Valls, Gap Spectroscopy